

Spring 5-2024

Characterization and Analysis of Supersonic Flow Through De Laval Nozzles at Varied Design Conditions

Sarah Baird

Embry-Riddle Aeronautical University, bairds4@my.erau.edu

Follow this and additional works at: <https://commons.erau.edu/edt>



Part of the [Aerodynamics and Fluid Mechanics Commons](#)

Scholarly Commons Citation

Baird, Sarah, "Characterization and Analysis of Supersonic Flow Through De Laval Nozzles at Varied Design Conditions" (2024). *Doctoral Dissertations and Master's Theses*. 796.

<https://commons.erau.edu/edt/796>

This Thesis - Open Access is brought to you for free and open access by Scholarly Commons. It has been accepted for inclusion in Doctoral Dissertations and Master's Theses by an authorized administrator of Scholarly Commons. For more information, please contact commons@erau.edu.

CHARACTERIZATION AND ANALYSIS OF SUPERSONIC FLOW THROUGH
DE LAVAL NOZZLES AT VARIED DESIGN CONDITIONS

By
Sarah Baird

A Thesis Submitted to the Faculty of Embry-Riddle Aeronautical University
In Partial Fulfillment of the Requirements for the Degree of
Master of Science in Aerospace Engineering

May 2024
Embry-Riddle Aeronautical University
Daytona Beach, Florida

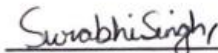
**CHARACTERIZATION AND ANALYSIS OF SUPERSONIC FLOW THROUGH
DE LAVAL NOZZLES AT VARIED DESIGN CONDITIONS**

By

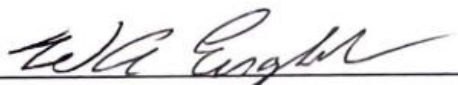
Sarah Baird

This Thesis was prepared under the direction of the candidate's Thesis Committee Chair, Dr. Surabhi Singh, Department of Aerospace Engineering, and has been approved by the members of the Thesis Committee. It was submitted to the Office of the Senior Vice President for Academic Affairs and Provost, and was accepted in the partial fulfillment of the requirements for the Degree of Master of Science in Aerospace Engineering.

THESIS COMMITTEE


Chair, Dr. Surabhi Singh


Member, Dr. Ebenezer Gnanamanickam


Member, Dr. William Engblom

Graduate Program Coordinator,
Dr. Hever Moncayo

Date

Dean of the College of Engineering,
Dr. James W. Gregory

Date

Associate Provost of Academic Support
Dr. Kelly Austin

Date

To Baxter

ACKNOWLEDGMENTS

I would like to thank my advisor, Dr. Singh, for her supervision and guidance during the course of my master's degree. The opportunity to work in her laboratory has transformed my attitude toward engineering. My gratitude extends to the faculty of Embry-Riddle Aeronautical University within the Department of Aerospace Engineering, particularly those within my thesis committee, Dr. Engblom and Dr. Gnanamanickam, for all they have taught me. I would like to thank my labmates and colleagues for a cherished time spent together in and outside of the lab. My appreciation also goes out to my family and friends for their encouragement and support all through my studies.

ABSTRACT

A combined numerical and experimental investigation of supersonic planar nozzles under different design conditions has been conducted. Supersonic planar nozzles are common geometries observed in supersonic wind tunnels and aircraft or rocket engines. For the important role they play in wind tunnel testing and aircraft propulsion, it is important to conduct a thorough numerical and experimental study to characterize their performance at different operating conditions. In this study, a de Laval nozzle was scanned to extract its contours and subsequently modeled to compare analytical and numerical performance expectations under design and off-design conditions. The nozzle was then installed in a supersonic blow-down wind tunnel to experimentally validate predicted effects of varying chamber pressure on nozzle performance, particularly within the overexpanded regime. Quantitative data in the form of wall pressure measurements and flow visualization via schlieren imaging were collected.

The investigation uncovered distinctive characteristics of overexpanded flow in planar nozzles, including internal separation and a well-defined shock structure. Decreasing the operating nozzle pressure ratio led to increased separation shock strength and more significant effects of overexpansion on nozzle performance and thrust capability. The shock interactions with the separated shear layer were evident, and downstream propagation of wave phenomena in the jet flow were observed. The design condition was simulated numerically, and while supersonic flow was present throughout the nozzle, some shocks were present in the nozzle flow leading to nonuniformities in the flowfield. To ensure reliable attainment of uniform design conditions, new nozzles with differing area ratios were designed and computationally validated. Three-dimensional numerical analysis ensured alignment with design requirements, including uniform core flow, minimal crossflow, and suitable turbulent boundary layer development. Nozzles have been developed for Mach 2 and 3 flow with the intent of creating a suitable test environment and studying these nozzle flows under design conditions.

TABLE OF CONTENTS

ACKNOWLEDGMENTS	i
ABSTRACT	ii
LIST OF FIGURES	vii
LIST OF TABLES	viii
1 Introduction	1
1.1 Motivation	1
1.2 Objectives	2
2 Background	4
2.1 The De Laval Nozzle	4
2.2 Nozzle Flow Patterns	6
2.3 Flow Processes in Overexpanded Nozzles	8
2.4 Supersonic Turbulent Boundary Layers	9
2.5 Wave Interactions with a Free Boundary	11
2.6 Flow Separation	11
2.7 Nozzle Flow Separation	13
2.8 Predicting Nozzle Internal Separation	14
2.9 Thrust	19
2.10 Nozzle Design	21
2.11 The Method of Characteristics	22
3 Nozzle Performance Analysis	24
3.1 Supersonic Nozzle	24
3.2 Facility	25
3.3 Experimental Approach	27

3.3.1	Experimental Setup	27
3.3.2	Schlieren Imaging	28
3.4	Experimental Results	30
3.5	Modeling Nozzle Geometry	38
3.6	Computational Approach	38
3.7	Design Condition	38
3.7.1	Numerical and Analytical Results	40
3.8	Overexpanded Condition	41
3.8.1	Numerical Results	42
4	Nozzle Design	44
4.0.1	Sivells' Method	45
4.0.2	Hopkins-Hill Method	48
4.1	Nozzle Design Criteria	50
4.2	Nozzle Contours	50
4.3	Computational Results	50
4.3.1	Three-Dimensional Computational Results	54
4.4	Component Integration/Assembly	58
4.5	Nozzle Comparison	61
5	Conclusions	64
5.1	Nozzle Overexpansion	64
5.2	Nozzle Design	66
5.3	Recommendations	67
6	REFERENCES	68
	REFERENCES	68
	PUBLICATIONS	72

LIST OF FIGURES

Figure	Page
1.1 Research Outline.	3
2.1 Inviscid nozzle pressure distribution.	9
2.2 Shock and expansion wave reflection from a free boundary.	11
2.3 Gradual velocity profile development when encountering a positive pressure gradient.	12
2.4 Conjecture on shock and fluid phenomena occurring within an internally separated region in an symmetric planar nozzle.	15
2.5 Thrust calculation in a nozzle via integration of pressure forces.	20
3.1 Supersonic nozzle.	24
3.2 Experimental facility located in LB182B.	25
3.3 Experimental setup.	28
3.4 Pressure tap locations.	29
3.5 Z-type schlieren setup.	29
3.6 Attainable steady-state times.	31
3.7 Pressure vs. position in nozzle, over NPR range.	32
3.8 Pressure ratio vs. position in nozzle, over NPR range.	32
3.9 Schlieren of separation zone, $p_0 = 76$ psia.	33
3.10 Separation shock strength vs. NPR.	33
3.11 Schlieren, variation in separation location at $NPR = 4.50$.	35
3.12 Schlieren, variation in separation location at $NPR = 5.16$.	35
3.13 Schlieren scaling.	36
3.14 Pressure distribution with silencer on and off, $p_0 = 66$ psia.	36
3.15 Pressure distribution with silencer on and off, $p_0 = 76$ psia.	36
3.16 Thrust vs. NPR.	37

3.17 Thrust Coefficient vs. NPR.	37
3.18 3-D scan output and resulting nozzle geometry.	38
3.19 Nozzle mesh.	39
3.20 Nozzle mesh around throat.	39
3.21 Contours of a) Mach number and b) static pressure, design condition ($p_0 = 110 \text{ psia.}$)	41
3.22 Contours of Mach number and static pressure, $p_0 = 66 \text{ psia.}$	43
3.23 Contours of Mach number and static pressure, $p_0 = 76 \text{ psia.}$	43
4.1 Regions of inviscid contour.	46
4.2 Reference boundary shape.	49
4.3 Mach 2 nozzle contour.	51
4.4 Mach 3 nozzle contour.	51
4.5 Mesh for Mach 2 nozzle.	52
4.6 Mesh for Mach 3 nozzle.	52
4.7 Contours of Mach number in Mach 2 nozzle through a) entire channel, b) test section ($p_0 = 45 \text{ psia.}$)	53
4.8 Contours of Mach number in Mach 3 nozzle through a) entire channel, b) test section ($p_0 = 100 \text{ psia.}$)	53
4.9 Contours of Mach number in Mach 2 nozzle along expanding width centerline plane through a) entire channel, b) test section ($p_0 = 45 \text{ psia.}$)	55
4.10 Contours of Mach number in Mach 2 nozzle along constant width centerline plane through a) entire channel, b) test section ($p_0 = 45 \text{ psia.}$)	55
4.11 Contours of Mach number in Mach 3 nozzle along expanding width centerline plane through a) entire channel, b) test section ($p_0 = 100 \text{ psia.}$)	56
4.12 Contours of Mach number in Mach 3 nozzle along constant width centerline plane through a) entire channel, b) test section ($p_0 = 100 \text{ psia.}$)	56

4.13	Contours of pressure in Mach 2 nozzle along expanding width centerline plane through a) entire channel, b) test section ($p_0 = 45 \text{ psia}$).	57
4.14	Contours of pressure in Mach 2 nozzle along constant width centerline plane through a) entire channel, b) test section ($p_0 = 45 \text{ psia}$).	57
4.15	Contours of pressure in Mach 3 nozzle along expanding width centerline plane through a) entire channel, b) test section ($p_0 = 100 \text{ psia}$).	58
4.16	Contours of pressure in Mach 3 nozzle along constant width centerline plane through a) entire channel, b) test section ($p_0 = 100 \text{ psia}$).	58
4.17	Centerline Mach distribution.	59
4.18	Centerline Mach 2 distribution.	59
4.19	Centerline Mach 3 distribution.	59
4.20	Contours of Mach number in Mach 2 nozzle along cross-sectional planes ($p_0 = 45 \text{ psia}$).	60
4.21	Contours of Mach number in Mach 3 nozzle along cross-sectional planes ($p_0 = 100 \text{ psia}$).	60
4.22	Nozzle solid model and assembly integration.	61
4.23	Mach 2.59 nozzle test section contours of Mach number.	62
4.24	Mach 2 nozzle test section contours of Mach number.	62
4.25	Mach 3 nozzle test section contours of Mach number.	62
4.26	Centerline Mach number, Mach 2.59 nozzle.	63
4.27	Centerline Mach number, Mach 2 nozzle.	63
4.28	Centerline Mach number, Mach 3 nozzle.	63

LIST OF TABLES

Table	Page
3.1 Nozzle geometry.	24
3.2 Location of separation shock	34
3.3 CFD Solver Parameters	39
3.4 Numerical and Isentropic Nozzle Exit Plane Parameters (Design condition, $p_{0inlet} = 110\text{ psia}$)	42
3.5 Comparison of Numerical and Experimental Shock Characteristics	42
4.1 Nozzle Design Parameters	51
4.2 CFD Solver Parameters	52
4.3 Numerical and Isentropic Test Section Parameters	54
4.4 Comparison of Numerical and Isentropic Exit Plane Conditions	60
4.5 Comparison of Old and New Nozzles	62

Nomenclature

δ	boundary layer thickness
δ^*	displacement thickness
\dot{m}	mass flow rate
γ	ratio of specific heats
μ	dynamic viscosity
ν	Prandtl-Meyer angle
ρ	density
τ	shear stress
θ	turn angle
A	area
a	speed of sound
A_1^*	nozzle throat area
A_d^*	diffuser throat area
C_F	thrust coefficient
F	thrust
M	Mach number
NPR	nozzle pressure ratio
p	pressure

R	gas constant
T	temperature
u	velocity
y	height above wall

Subscripts

0	total conditions
a	ambient conditions
e	exit conditions
i	ideal conditions under perfect expansion
s	conditions upstream of separation
t	throat conditions

1 Introduction

This project was undertaken in the effort to assist in fulfilling the commissioning of a compressible aerodynamics laboratory and high-speed wind tunnel for educational and research usage by Embry-Riddle Aeronautical University.

1.1 Motivation

Understanding and optimizing the aerodynamic performance of supersonic air vehicles is essential for enhancing their efficiency, stability, and safety. Among the critical aspects of supersonic aerodynamics, the behavior of converging-diverging nozzles is particularly significant due to their complex behavior and wide-ranging applications, including supersonic wind tunnels. Nozzles integrated within supersonic wind tunnels must generate a uniform, disturbance-free supersonic test environment suitable for precise study of high-speed aerodynamics. Off-design supply conditions have dramatic effects on nozzle performance and internal flow behavior. Overexpanded conditions are routinely encountered in flight, whether in rocket or jet nozzles, and so it is important to understand nozzle flow physics at different design conditions and the real effects these variations have.

Boundary layers form along all aircraft surfaces and play a crucial role in the interaction between the aircraft and the surrounding flow field. In the context of supersonic flight, these boundary layers undergo unique characteristics that significantly differ from their subsonic counterparts. The variation in upstream pressure supplied to a nozzle introduces distinct flow phenomena, including compressibility effects, flow separation, shock wave-boundary layer interactions (SWBLI), and development of turbulent structures [? ? ?]. Boundary layer interactions with high-speed flow patterns can produce regions of high pressure and surface stresses; it is therefore important to reproduce these conditions in a controlled environment to better understand the flowfield.

In the application of supersonic wind tunnels, nozzle design must be performed very meticulously to ensure a clean, uniform flow at the nozzle exit plane. It is desirable to expand the flow isentropically, with no shocks in the nozzle, so that the flow leaving nozzle

has consistent velocity and lacks angularity. This allows for a close replication of in-flight conditions in the test section so that models may be tested with accuracy.

1.2 Objectives

The primary objective of the current work is to deepen our understanding of supersonic nozzle flows, particularly the viscous effects on overexpansion and shock interactions that form within them in this regime. This will encompass the characterization of supersonic nozzle flows and examination of the impact of various parameters, such as nozzle pressure ratio (NPR) and geometry, on the flow behavior.

The means to achieve these goals are outlined in Fig 1.1. The primary objective of the work is to characterize the internal flow of de Laval nozzles under varied design conditions to better understand their performance under off-design conditions and also enhance their design for use in high-speed wind tunnels. The internal flow through a nozzle will be computationally simulated for a range of NPRs, and results validated using experimental techniques on a blowdown-type supersonic wind tunnel. Static pressure measurements and schlieren imaging will be performed to capture and analyze nozzle flow, particularly the viscous effects at off-design conditions and the resulting flow separation and shock formation within the nozzle. The unsteady characteristics defining shock-induced separation patterns will be studied inside a planar nozzle, and the changes in behavior over a range in NPRs will be analyzed, particularly within the overexpanded regime. The effect of NPR on separation structure, flow asymmetry, thrust, shock strength, and separation location will be investigated.

Additionally, new nozzles will be designed and computationally analyzed, so the effects of changes in area ratio and design Mach number on nozzle performance may also be studied. Nozzles will be designed to satisfy facility constraints and nozzle requirements so that they may eventually be integrated and tested successfully. The final expectation of this investigation is to examine the impact of nozzle operating conditions on performance so that nozzle behavior may be better understood and controlled.

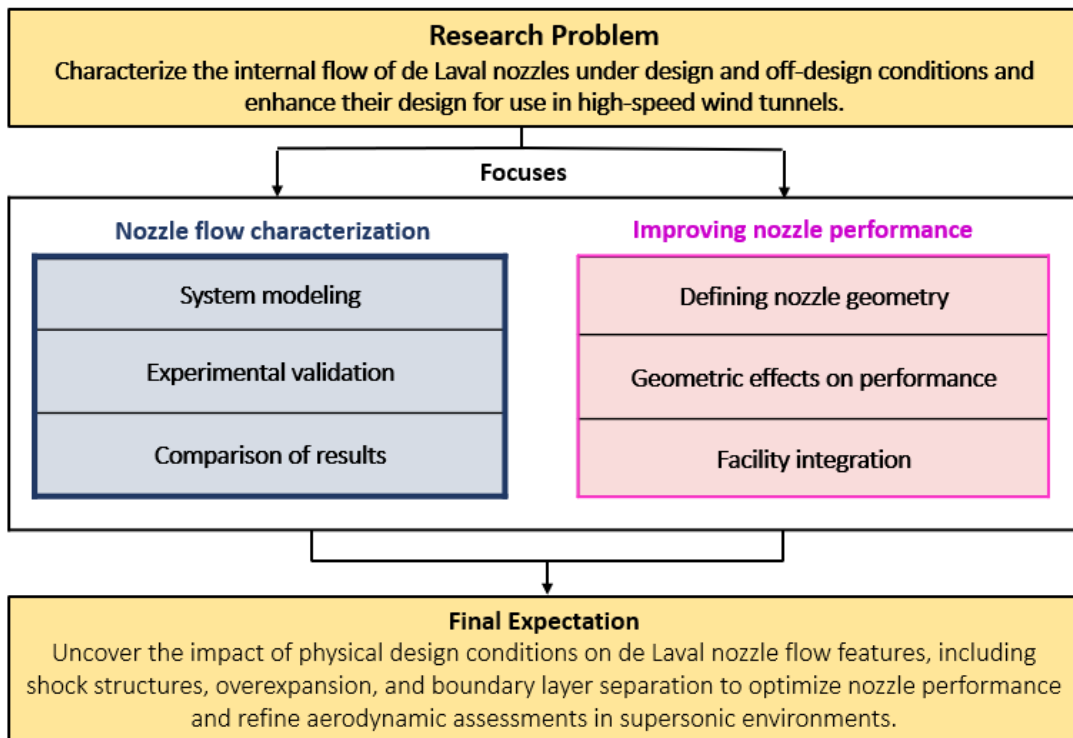


Figure 1.1 Research Outline.

2 Background

This section serves to provide a theoretical foundation for the mathematical and aerodynamic principles used to describe high-speed compressible nozzle flows that have been used in this project. Published literature describing similar investigations is publicly available and will be referenced as appropriate.

2.1 The De Laval Nozzle

The de Laval nozzle, also known as a converging-diverging nozzle, is a key component used in supersonic flow systems. It is designed to accelerate and expand a flow to supersonic speeds effectively and efficiently. The de Laval nozzle consists of two main sections: the converging section and the diverging section. The converging section compresses the initially subsonic flow, causing it to accelerate. The converging section is designed to ensure smooth, streamlined flow as the flow is further accelerated to the desired Mach number.

After reaching the throat of the nozzle, which is the narrowest point, the flow enters the diverging section. In this section, the flow expands gradually, allowing it to reach supersonic speeds. As the cross-sectional area increases, there is a resulting in an increase in velocity now that the flow has surpassed the speed of sound. The diverging section is specifically shaped to ensure that the flow expansion occurs gradually so that pressure losses are minimized.

This reversal in flow physics from the subsonic to supersonic regime can be explained through the governing equations of the flow [?]. Starting with the continuity equation, which establishes the conservation of mass:

$$\dot{m} = \rho u A = \text{constant} \quad (2.1)$$

Deriving this equation:

$$u A * d\rho + \rho A * du + \rho u * dA = 0 \quad (2.2)$$

and dividing by mass flow rate yields:

$$\frac{d\rho}{\rho} + \frac{du}{u} + \frac{dA}{A} = 0 \quad (2.3)$$

Next, we will turn to the conservation of momentum:

$$\rho u * du = -dp \quad (2.4)$$

Using an isentropic flow relation:

$$\frac{dp}{p} = \gamma p \frac{d\rho}{\rho} \quad (2.5)$$

and the equation of state:

$$p = \rho RT \quad (2.6)$$

we obtain:

$$dp = \gamma RT * d\rho \quad (2.7)$$

Now using the definition of the speed of sound, $a = \gamma RT$:

$$dp = a^2 d\rho \quad (2.8)$$

Substituting this expression for the change in pressure into the momentum equation, and using the definition of Mach number, $M = ua$:

$$\rho u * du = -(a^2) d\rho \quad (2.9)$$

$$\frac{u}{a^2} * du = \frac{-d\rho}{\rho} \quad (2.10)$$

$$-(M^2) * \frac{du}{u} = \frac{d\rho}{\rho} \quad (2.11)$$

Finally, substituting this expression for $d\rho/\rho$ back into the continuity equation:

$$-(M^2) * \frac{du}{u} + \frac{du}{u} + \frac{dA}{A} = 0 \quad (2.12)$$

$$(1 - M^2) * \frac{du}{u} = -\frac{dA}{A} \quad (2.13)$$

This gives a final relationship between incremental changes in velocity and area, dependent on the Mach number. It is clear that for a subsonic flow ($M < 1$), the term $(1 - M^2)$ is positive, and an increase in area will produce a decrease in velocity. Conversely, if the flow is supersonic ($M > 1$), the term $(1 - M^2)$ is negative, and an increase in area will produce an increase in velocity. This can be intuitively explained due to the compressibility effects present in supersonic flow. In a subsonic flow, the density remains relatively constant, so the change in area must be countered by a change in velocity so that mass is conserved; however, in supersonic flows, the density is variable and it changes along with velocity as area is altered. The equation developed from the conservation of momentum,

$$-(M^2) * \frac{du}{u} = \frac{d\rho}{\rho} \quad (2.14)$$

shows that for supersonic flows, that is, at Mach numbers greater than 1, the change in density is much larger than the change in velocity. Therefore, in order to satisfy conservation laws in a supersonic flow, as the area is increased, the density decreases and the velocity increases. This is the working principle behind the converging-diverging nozzle.

2.2 Nozzle Flow Patterns

The operating conditions to which a supersonic nozzle is subjected play a critical role in determining the internal flow features and expansion of the working fluid. Gas stored

in a high-pressure chamber is released through the nozzle and exhausted into a region of low pressure. This pressure difference, or favorable pressure gradient, is what drives the flow through the nozzle. The magnitude of this pressure difference is used to define the nozzle operating conditions, and is referred to as the expansion ratio, defined to be the total chamber pressure divided by the static pressure at the nozzle exit plane. The flow is also affected by the nozzle pressure ratio (NPR), defined to be the total chamber pressure divided by the ambient pressure into which the nozzle is exhausted. At the ideal “design condition”, the flow through the nozzle is said to be perfectly expanded. At this condition, the pressure at the nozzle exit plane is equal to the back pressure into which the fluid is exhausted, and the flow is nominally isentropic. As the NPR is lowered, i.e. as the inlet total pressure is lowered or the back pressure is increased, the flowfield deviates from this ideal condition and irreversible processes can occur within the nozzle, resulting in significant losses in energy and total pressure [?]. The changes in the flow pattern due to fluctuations in the ratio of exit to chamber pressure are predictable, and distinct flow regimes can be defined, as shown in Fig. 2.1.

At low chamber pressures, the flow through the nozzle will be entirely subsonic. The flow accelerates through the converging section of the nozzle and decelerates through the diverging section of the nozzle.

Assuming the back pressure is held constant, if the chamber pressure is increased enough, the flow will be choked. The “choked” condition is obtained when the flow reaches Mach 1, or the local speed of sound, at the throat, where the nozzle area is a minimum. At the choked condition, the flow will again decelerate through the diverging portion of the nozzle, although the flow will have lower static pressure in this region than the purely subsonic case.

If the chamber pressure is further increased, a region of supersonic flow will form in the diverging section of the nozzle. Contrasting from subsonic flow, supersonic flow will accelerate as it is expanded, as mentioned previously. This region of supersonic flow will be abruptly halted by the presence of a normal shock. As the chamber pressure is increased,

the position of this normal shock will move downstream until it reaches the nozzle exit. At this point, the flow inside the nozzle will be entirely supersonic, however, after the shock, the jet flow velocity will still be subsonic.

If the chamber pressure is increased further, it will reach an overexpanded condition. The pressure at the exit of the nozzle is lower than the back pressure, and the effects of this phenomenon manifest in a complex pattern of shocks and reflected wave phenomena in the jet flow. This condition is the primary flow region of interest in this study, and will be later described in more depth.

Once the chamber pressure is sufficiently increased, the design condition will be reached and the flow will be perfectly expanded. The flow will be uniformly supersonic, and the wave phenomena in the jet flow will vanish.

If the chamber pressure is increased past the design point, the nozzle will enter an underexpanded case. Because there is once again an imbalance between the pressure at the nozzle exit and the ambient back pressure, with the exit pressure being higher than the back pressure, expansion waves will form at the nozzle exit, and the flow at the edges of the jet will turn outward, causing a distinct wave pattern outside of the nozzle.

All of these expansion cases are dependent on the nozzle pressure ratio. When the flow accelerates, whether in the subsonic or supersonic regime, the static pressure will decrease. Over a shock, there will be a sharp gradient in flow parameters, with the static pressure and density increasing, and the velocity decreasing. The expectations of flow behavior for each of these cases can be predicted assuming inviscid flow through the nozzle. In reality, viscous effects significantly affect the flow behavior at each of these conditions, particularly in the overexpanded regime.

2.3 Flow Processes in Overexpanded Nozzles

When the nozzle flow is overexpanded, the pressure at the nozzle exit is lower than the back pressure. Since the flow must compress rapidly to equalize with the back pressure, the inviscid flow model predicts that oblique shocks will form outside of the nozzle in this regime.

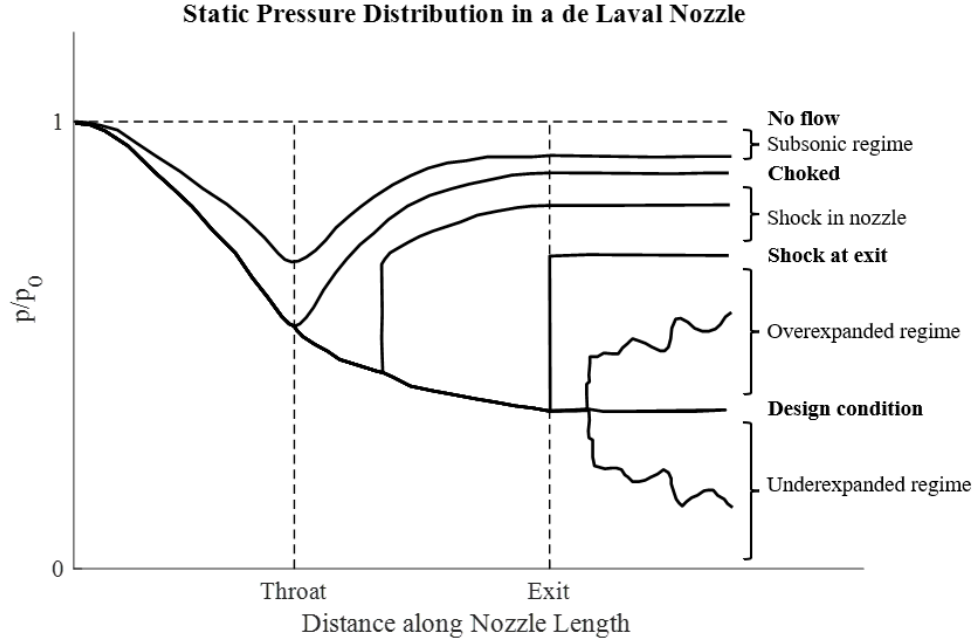


Figure 2.1 Inviscid nozzle pressure distribution.

Experimentation has shown that the effects of overexpansion can manifest in different ways, particularly in internal flow separation. The boundary layer of the nozzle detaches from the nozzle wall in this case, and a recirculation region forms a thick shear layer. The result is a complex turbulent structure, with wave phenomena consisting of shock waves and expansion fans reflecting off of the free boundary of the shear layer. The effects of nozzle pressure ratio on the severity of overexpansion are significant. As the NPR is lowered, the overexpansion becomes more severe, and at low enough NPRs, the shock structure will move inside the nozzle, a phenomenon which holds drastic impact on nozzle performance. This phenomenon is not well understood and is challenging to predict computationally; because of the variation in NPR faced in supersonic flight, the implications of this effect must be studied further so that non-optimal nozzle flows may be predicted and controlled more accurately.

2.4 Supersonic Turbulent Boundary Layers

The boundary region between two flows with notably different velocities is called a shear layer. The flow faces a significant velocity gradient, contributing to an increase in viscous

shear stress, defined by the following relationship:

$$\tau = \mu \frac{du}{dy} \quad (2.15)$$

The most familiar type of shear layer is the boundary layer over a solid body immersed in a fluid. Under no-slip conditions, the fluid must be stagnant at the surface of an impenetrable object, and so there is a thin region where the flow transitions from rest to the “free-stream” velocity. This region, the boundary layer, is a thin layer of fluid that forms on the surface of any object moving through a fluid medium. In the case of supersonic flow, the boundary layer experiences significant changes due to the high speeds involved. Supersonic boundary layers are characterized by a sudden increase in pressure as the fluid is slowed from supersonic to subsonic speeds. This potentially causes the boundary layer to become more turbulent than in subsonic flows, and the higher velocity gradient leads to increased skin friction. The effect of compressibility on wall turbulence are relatively small in supersonic flows as opposed to hypersonic flows, and the heat transfer effects are expected to be limited in supersonic blowdown facilities, so the wall conditions can be assumed to be adiabatic [?]. The shear layer growth rate has been shown to decrease with increasing Mach number [?]. Another important feature of supersonic boundary layers is their behavior when interacting with shock waves, which form as these supersonic flow features encounter the surface of the object and can cause significant changes in the flow properties, including pressure, temperature, and velocity.

When the interface is not over a solid surface immersed in a fluid, this layer is referred to as a free shear layer, and it is not attached to a solid boundary. This is a characterizing constituent of separated supersonic flow, in which the boundary layer becomes detached from the solid surface and the free shear layer exists some distance away from the wall. In the region between the free shear layer and the wall, or recirculation zone, the flow moves at a relatively low velocity. On the other side of the free shear layer lies the free-stream flow, moving at a higher velocity and usually possessing a lower level of vorticity. The shear layer

itself is very thin and possesses a high level of turbulence [?].

2.5 Wave Interactions with a Free Boundary

When a shock wave impinges on a free shear layer, rather than being reflected as a shock wave as it would from a solid boundary, it is instead reflected as an expansion wave. Similarly, an expansion wave will reflect from a free boundary as a shock wave. While the velocities on either side of a free shear layer will be different, the pressure across this boundary must be constant, and therefore, the incident waves must reflect in this manner so as to maintain this pressure. In the diverging section of a nozzle, the separated shear layer behaves in this fashion. The shock and the expansion waves will deflect the flow, and the shear layer will also deflect in the same direction. Therefore, the shape of the shear layer may not be constant, as it is not a fixed boundary and is allowed to bend in order to adhere to the flow generated by the angled shock and expansion waves [?], as shown in Fig. 2.2. The reflected waves form a diamond pattern as they propagate downstream, an expected characteristic of overexpanded flow.

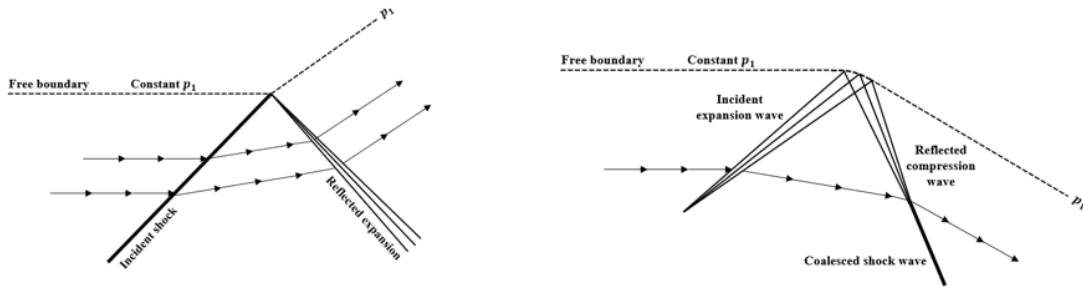


Figure 2.2 Shock and expansion wave reflection from a free boundary.

2.6 Flow Separation

Flow separation refers to the phenomenon where a flow detaches from a solid surface, causing a disruption in the smooth flow pattern. The flow no longer follows the contour

of the surface and separates, creating a region of reversed or chaotic flow. Flow separation typically occurs when there is a significant adverse pressure gradient, curvature, or flow acceleration along a surface. When the flow encounters such conditions, the pressure on the surface increases, slowing down the flow near it, as seen in Fig. 2.3. As a result, the velocity gradient in the wall normal direction becomes zero, leading to boundary layer separation. Generally, at higher Reynolds numbers, the greater the adverse pressure gradient must be to induce separation, as the velocity profile will become more blunt. [?]

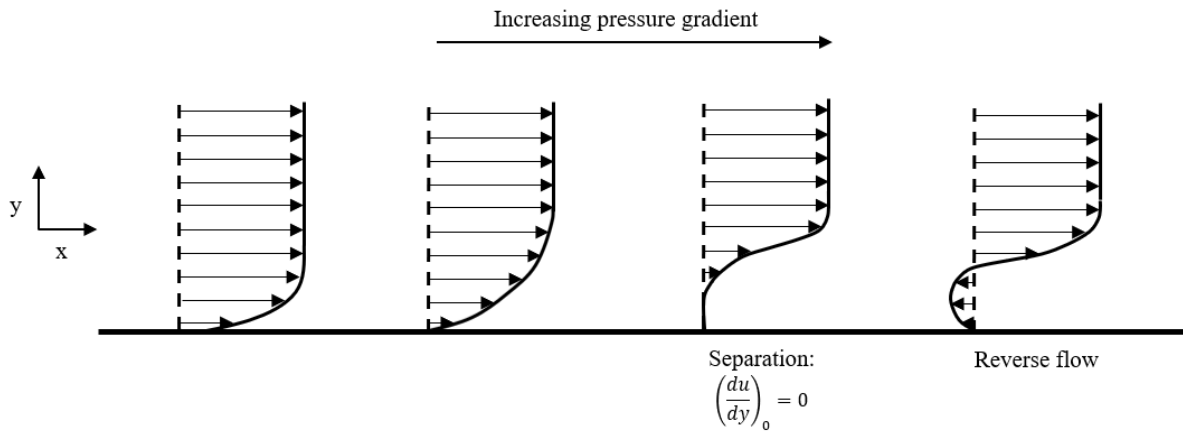


Figure 2.3 Gradual velocity profile development when encountering a positive pressure gradient.

Laminar boundary layers are typically more likely to separate than turbulent boundary layers due to a lower characterizing wall shear stress, although separation can occur in both laminar and turbulent flows. In laminar flows, separation results in the formation of a recirculation zone where the flow moves in a reverse direction. In turbulent flow, the separated flow becomes highly turbulent and unsteady, characterized by vortices and eddies. Flow separation has several implications and consequences. It leads to an increase in drag on the object or surface, reducing its overall efficiency. It can also cause loss of lift, reducing the stability and control of aerodynamic surfaces, such as wings or airfoils. It is desirable, then, to minimize flow separation both in the nozzle itself, and use it to study the causes and effects of flow separation in high-speed vehicles.

Supersonic wind tunnel nozzle design must be done carefully to gradually expand the flow without causing flow separation or forming any strong shocks in the nozzle interior. In a thoughtfully designed supersonic nozzle, the boundary layer will transition to turbulence prior to the start of the diverging section. This is to avoid any disturbances in the flow in the supersonic portion of the nozzle, as any perturbations will propagate significantly in supersonic flow, decreasing the uniformity of the flowfield, which is an essential characteristic in wind tunnel applications. In rocket nozzle applications, viscous effects also normally result in the development of a turbulent boundary layer. Due to the intended applications in wind tunnel and rocket nozzles, turbulent flow separation will be discussed herein.

2.7 Nozzle Flow Separation

If a supersonic nozzle is exhausted to an ambient pressure that is greater than the exit pressure to which the nozzle is designed, the nozzle jet flow will contain oblique shocks, and may separate off the internal walls of the nozzle if the pressure difference is great enough. Separation occurs in nozzles operating at NPRs below the design condition, and as such are a result of the pressure difference driving overexpansion as the flow compresses rapidly to equalize with the back pressure. As the severity of overexpansion is increased, separation is found to occur in the diverging portion of a nozzle when the wall pressure is reduced to 20-50% of the surrounding pressure [?]. The boundary layer can only remain attached within a certain differential pressure; if the pressure increase is severe enough, the boundary layer will separate from the nozzle wall. The boundary layer thickens, and a slanted shock forms which extends into the boundary layer. The pressure increase over this shock raises the static pressure of the flow almost to the back pressure, with the remaining increase occurring between the shock and the nozzle exit. This generated adverse pressure gradient causes the boundary layer to detach at the separation point. This differs from the inviscid prediction of sharp compression, which assumes a normal shock sitting in the nozzle.

The flow phenomena commonly associated with shock-induced separation occurring as a result of overexpansion are shown in Fig. 2.4. The shock driving the separation is referred

to as the separation shock, and thus this phenomenon can be referred to as shock-induced flow separation [?]. Separation shocks will form on the top and bottom walls in a planar nozzle. These shocks will intersect somewhere near the nozzle centerline, connected by a perpendicular normal shock, called the Mach stem. Flow patterns behind the shocks are complex and host a variety of interactions between turbulent structures that make up the flow. Immediately behind the Mach stem, the flow will be locally subsonic in the slipstream. Because of the decrease in total pressure over a shock, the sonic area required to choke the flow will increase, and so the flow will soon again become supersonic due to the artificial throats formed by the now much thicker shear layer boundary. The separation shocks intersect with the Mach stem at the triple point, which produce reflected shocks, which are then reflected from the free boundary as expansion waves, which again intersect to form reflected shocks, and so on until the reflected wave phenomena reach the nozzle exit. A thick recirculation region forms in the separated shear layer region near the wall. Often, one lambda foot of the separation shock will be larger than the other, even in flow separation occurring in symmetric nozzles. The shear layer stemming from the large lambda foot has been shown to grow rapidly and display strong instabilities, while the shear layer stemming from the small lambda foot grow at a much slower rate [?]. Additionally, overexpanded nozzles are seen to be highly unsteady, with the separation location oscillating in the longitudinal direction [?].

2.8 Predicting Nozzle Internal Separation

Flow separation in a supersonic nozzle is a regularly occurring fluid phenomenon, although the large discrepancy between the behavior predicted by 1-D quasi-inviscid theory and the actual flow behavior make this hard to predict, and not well understood. Therefore, the consideration of viscous effects is essential for accurately predicting overexpanded nozzle behavior and the tangible effects on lift, thrust, and stability that this condition induces. In the context of rocket motor performance, it is desirable to prevent or delay flow separation because of the instabilities this conditions induces, which lead to oscillating and asymmetric

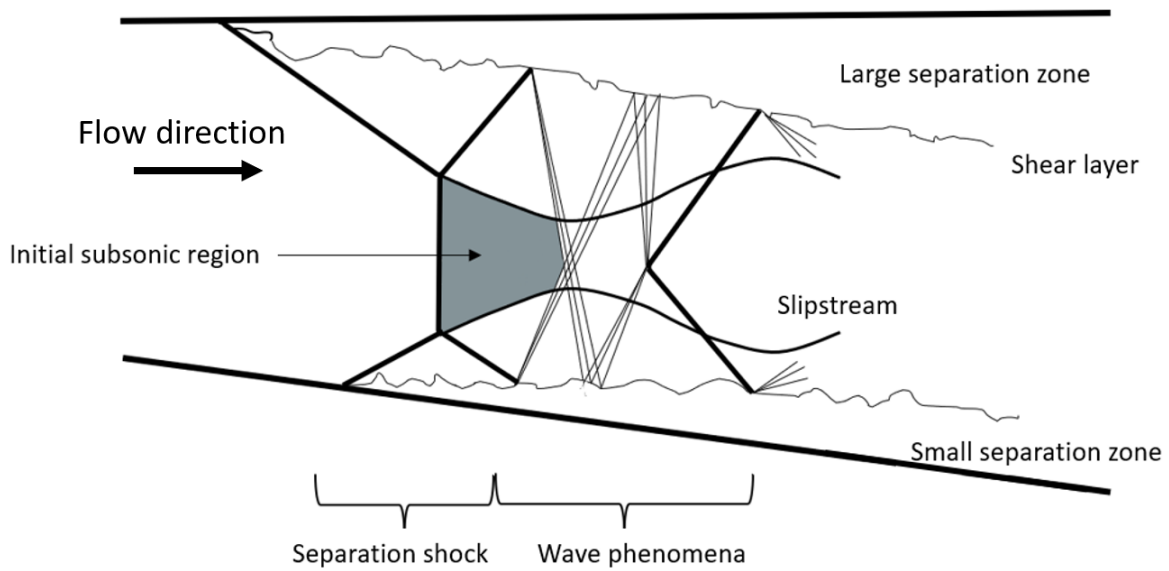


Figure 2.4 Conjecture on shock and fluid phenomena occurring within an internally separated region in an symmetric planar nozzle.

forces which can damage engine mountings that are held stationary in test environments [?].

Nozzle separation was first noticed in the early 20th century with the implementation of the steam turbine, however there was no criteria established for predicting the onset of this phenomenon. Detailed work into separation prediction commenced as efforts in the development of rocket propulsion began to rapidly accelerate in the 1940s. Early studies found that separation was dependent on the ratio of pressure upstream of the separation to that of the back pressure. Most studies found separation to be independent of nozzle divergence angle, ratio of specific heats, and gas temperature. Of the early investigations, the results of Scheller and Bierlein [?] conflicted in that they stated the pressure ratio at which separation would occur was reliant on nozzle divergence angle, and also that Reynolds number played an impactful role in delaying separation, but their lack of data prevented any definitive correlations from being made.

Since it is desirable to predict the behavior of overexpanded nozzles, there have been many notable modern efforts to determine the most accurate computational models for

doing so. Much of the current literature focuses on separation in rocket nozzles, which are axisymmetric. Two-dimensional, or planar, nozzles has been found to be quite challenging, due to the three-dimensional effects that manifest from the shock-boundary layer interactions and distinct flow separation that form in these systems [?]. In regards to predicting the behavior of separated nozzle flows, parameters of interests include primarily the strength of the separation shock, defined by the change in pressure over this shock, and the wall separation location. Shock strength has been shown to be predictable to some degree of accuracy using standard computational turbulence models, while separation location is a more difficult parameter to predict accurately.

A number of parameters governing nozzle separation have been introduced by various investigators. The separation pressure ratio (p_s/p_a) is defined to be the ratio of the nozzle wall pressure just upstream of the separation to the external back pressure. Recent studies have suggested the primary correlations of the separation pressure ratio to be the following, with the subscript s denoting the undisturbed value just upstream of the separation.

$$\frac{p_s}{p_a} = f\left(\frac{p_0}{p_a}\right) \quad (2.16)$$

and

$$\frac{p_s}{p_a} = f(M_s) \quad (2.17)$$

The two equations can be linked through isentropic relations, with the Mach number ahead of the separation being a function of the pressure ratio p_s/p_0 and the ratio of specific heats (γ).

It has been shown that the effect of γ is not apparent from available data, however Lawrence [?] attained a better correlation using the second equation than the first, due to the Mach number being more closely related to the local conditions at the boundary layer separation than the wall static pressure. Lawrence also found that separation in longer con-

toured nozzles occurred at lower chamber pressures than in nozzles with higher expansion angles. The possible cause of this was identified to be the reduction of the effective pressure downstream of the separation caused by the entrainment of the air in the separated circulation region.

If a traditional boundary layer separation approach is considered, separation occurs when the flow is subjected to an adverse pressure gradient. The velocity profile will gradually change, transitioning from laminar to turbulent, and eventually separating when the adverse pressure gradient results in a reversal of the flow, as described previously. Separation may predicted from the boundary layer equations by specifying the pressure gradient and locating the point at which the velocity at the wall changes direction. For the problem of determining separation point in a supersonic nozzle, this method is not directly applicable, as there is a sharp discontinuity in the pressure across the separation shock, and the pressure gradient cannot be specified directly. Romine [?] developed an analytical model to pinpoint separation pressure and location by performing a balance of pressure and flow direction and the triple point, which aligned with data collected for short nozzles, but a widely applicable model for low divergence angle nozzles has yet to be developed.

Morrisette and Golberg [?] collected experimental data for a variety of nozzles and found that zero-pressure-gradient separation predictors can return fairly reasonable estimations of separation location, notably the semi-analytical procedure developed by Reshotko and Tucker [?]. This method is conceptually based on the notion that in supersonic flows, the free-stream Mach number has a large effect on the boundary layer velocity profile. A relationship between the Mach number and the velocity profile is established, and then the change in Mach number across the separation shock can be analytically determined from the boundary layer form factors, specifically the momentum and boundary layer thicknesses, for an incompressible turbulent boundary layer before and after the separation. The compressible boundary layer equations are transformed to the same form as the incompressible boundary layer equations, and then criteria governing incompressible separation is applied to

the modified compressible equations to develop an estimation of the range of Mach number ratio ahead of and behind the shock, from which the range of pressure ratios from which separation will occur can be extracted.

The Mach number at separation can be determined analytically from measured pressure data using the following isentropic flow relation:

$$M_s = f\left(\gamma, \frac{p_s}{p_0}\right) \quad (2.18)$$

Roshotko and Tucker’s method returns reasonable predictions for nozzles with large divergence angles; however, prediction of the separation point in nozzles with low divergence angles, such as contoured nozzles or wind tunnel nozzles, remains elusive due to the closeness of the separated shear layer to the wall, and thus drives the motivation to continue the experimental investigation of these flows and determine the most reliable submodels for predicting this phenomenon.

The accuracy of different turbulence models has been assessed in multiple computational studies. Current literature agrees on the shock structure associated with internal separation, with the angled incident shocks connected by the Mach stem, which are in turn reflected off the separated shear layer. Hamed and Vogatzis [?] found the k-omega model to be fairly accurate when predicting pressure ratio over the separation shock, however unable to predict the separation location with accuracy. At higher overexpanded nozzle pressure ratios, these predictions are more accurate, and corresponding thrust coefficients very close to experimentally obtained data. However, when the NPR is lowered further to severely overexpanded conditions, the unsteady effects make these predictions harder, and numerical projections diverge from the experimental data. In general, two-equation turbulence models are shown to provide the best overall agreement with experimental results in both the nozzle pressure distribution and the thrust values. Yaravintelimath [?] studied the SST model in depth in the context of its application to nozzle overexpansion and separation, and also found a sensitivity to NPR and type of nozzle, failing to predict the separation location.

The cause of this was concluded to be the limiting of the shear stress inside the boundary layer and overprediction of the jet spreading rate. By modifying the turbulence model, he was able to confirm that accurate prediction of this phenomenon is reliant on the correct jet spreading rate, and so experimental data must be used to empirically inform the coefficients of this model for accurate prediction of separation.

One of the most comprehensive studies has been performed by Hunter [?], who combined experimental and computational results on two-dimensional overexpanded flows. His experimental results showed the distinction of two regimes. At low NPRs, there was three-dimensional separation with partial reattachment, and at high overexpanded NPRs, there was two-dimensional fully detached separation. This is stated to be the result of the natural tendency of a nozzle operating in the overexpanded regime to detach for a more efficient thermodynamic balance. The result of this finding is when the nozzle flow separates, it is reflected in the performance, with a higher thrust than predicted by inviscid calculations.

2.9 Thrust

The thrust produced by the nozzle is an important characteristic defining nozzle performance. Predictions of thrust in overexpanded nozzles are challenging, however can be estimated computationally and analytically from experimental wall static pressure data. The effects of overexpansion induce losses into the system that will reduce the attainable thrust of a given nozzle, and at high-speed flight, even a small reduction in thrust coefficient can induce a large reduction in net thrust force [?]. Therefore, the reliable prediction of the flowfield is essential to characterizing flight performance under these operating conditions. Geatz [?] worked to develop a code to predict nozzle internal performance to predict thrust in a two-dimensional nozzle, and while applicable to a wide variety of nozzle geometries, still significantly underpredicted experimental thrust in cases of flow separation.

Papamoschou [?] introduces a derivation relating the NPR to the nozzle thrust, stemming from the definition of thrust as the axial component of the forces acting on the internal and external walls of the nozzle and supply chamber. An analytical approximation of nozzle

thrust can be determined by integrating the pressure forces acting on the nozzle walls in the axial direction. The nozzle surface is defined by the coordinate s , and the local surface inclination with respect to the horizontal (direction of thrust) is denoted by θ , as shown in Fig. 2.5. With this notation, the thrust of the nozzle can be defined as:

$$F = \int_o^e (p - p_a) \sin \theta \, ds \quad (2.19)$$

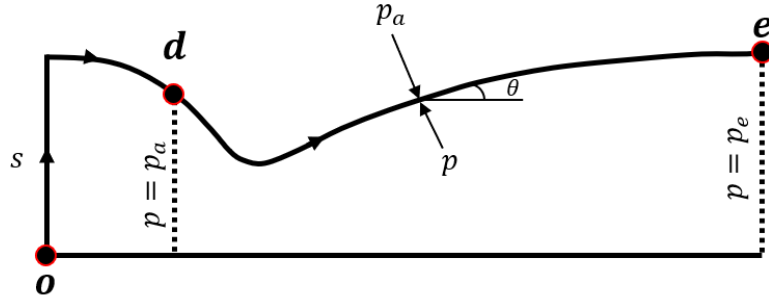


Figure 2.5 Thrust calculation in a nozzle via integration of pressure forces.

This constitutes the thrust through the entire nozzle. The nozzle channel can be divided into two portions, interfaced by the point at which the static pressure inside the nozzle is equal to the ambient back pressure. Dividing this integration over each region yields:

$$F = \int_o^d (p - p_a) \sin \theta \, ds + \int_d^e (p - p_a) \sin \theta \, ds \quad (2.20)$$

The first term represents the ideal thrust of the nozzle, as the flow is perfectly expanded when the nozzle pressure is equivalent to the back pressure, equal to the momentum flux corresponding to this condition.

$$F_i = \int_o^d (p - p_a) \sin \theta \, ds = \dot{m} u_e \quad (2.21)$$

Substituting this simplification into the thrust equation allows for a final formulation of

the thrust equation:

$$F = \dot{m}u_e + \int_d^e (p - p_a) \sin \theta \, ds \quad (2.22)$$

This quantity can be nondimensionalized by the ideal thrust to yield the thrust coefficient:

$$C_F = \frac{F}{F_i} = 1 + \frac{1}{\dot{m}u_e} \int_d^e (p - p_a) \sin \theta \, ds \quad (2.23)$$

Here, \dot{m} refers to the maximum mass flow rate value in the nozzle, which occurs at the throat and can be determined from the sonic conditions in the nozzle:

$$\dot{m} = A_t \gamma \frac{p_0}{a_0} \left(\frac{\gamma + 1}{2} \right)^{\frac{\gamma+1}{1-\gamma}} \quad (2.24)$$

The reservoir speed of sound (a_0) is determined from chamber conditions: $a_0 = \sqrt{\gamma R T_0}$. The nozzle exit velocity after the flow has been fully expanded can be determined using the nozzle pressure ratio:

$$u_e = a_0 \sqrt{\frac{2}{\gamma - 1} \left(1 - NPR^{\frac{(1-\gamma)}{\gamma}} \right)} \quad (2.25)$$

In order to solve for the thrust using this equation, the local pressure must be integrated through the nozzle after the air has been expanded past the design point up until the exit. This is done using an array of wall pressure data. If the nozzle geometry is known, the corresponding local inclination angles can be easily determined. This method will be utilized to calculate nozzle thrust and the results will be compared to direct thrust calculation to quantify the limitations of this analytical method.

2.10 Nozzle Design

There are two primary types of nozzles: minimum length and gradual expansion. Minimum length nozzles are usually implemented in rocket nozzle designs, where saving weight and size is usually prioritized above attaining a uniform flowfield at the nozzle exit plane. In the application to supersonic wind tunnels, turning angles are kept lower and a

longer flow straightening section is implemented to produce as high of flow quality as can be attained leaving the nozzle and supplying the test section [?]. To achieve the desired characteristics in a supersonic wind tunnel nozzle, important design considerations include:

1. **Throat area:** The nozzle throat area must be carefully designed to achieve a critical flow condition, known as choked flow, where the flow velocity reaches the speed of sound.
2. **Convergence and divergence angles:** The angles of the converging and diverging sections play a crucial role in controlling the flow expansion and acceleration. Optimal angles are chosen to minimize losses, prevent flow separation, and ensure smooth flow transition.
3. **Shock-free design:** It is desirable to design the nozzle in a way that minimizes the occurrence of shock waves and flow separation. This can be achieved through careful shaping of the converging and diverging sections, as well as consideration of the flow conditions.

By considering these factors, as well as meeting dimensional constraints, a well-designed supersonic wind tunnel nozzle can provide efficient and uniform supersonic flow, allowing for accurate and reliable testing of aerodynamic models and components.

2.11 The Method of Characteristics

The method of characteristics (MOC) is a mathematical technique involving the construction of characteristic lines or curves that represent the paths along which information propagates through the flow field. It is used to define the geometry of the diverging section of supersonic nozzles. The characteristics are determined by the flow properties at each point and provide a framework for solving the governing equations. The Prandtl-Meyer function is a mathematical relationship that describes the change in flow properties, such as Mach number and flow angle, across an expansion wave [?]. It relates the flow properties before

and after the expansion. The total deflection necessary to accelerate the flow to a desired Mach number may be determined using the Prandtl-Meyer angle, shown in Eq. 2.26. This is implemented incrementally through MOC in the MATLAB and FORTRAN code used to design the nozzles.

$$\nu = \sqrt{\frac{\gamma+1}{\gamma-1}} * \arctan \sqrt{\frac{\gamma-1}{\gamma+1}(M^2-1)} - \arctan \sqrt{M^2-1} \quad (2.26)$$

By tracking the characteristics, the changes in flow properties across the expansion fan can be determined. MOC produces two solutions, for subsonic and supersonic flow. For the calculations in nozzle design, the subsonic solution is discarded since the flow has been choked to obtain supersonic conditions at the throat prior to the diverging section.

An extension of MOC has been developed for contoured nozzles by Sivells [?], and will be discussed in more detail in Chapter 4.

3 Nozzle Performance Analysis

The first phase of this study centers around the investigation of an asymmetric planar nozzle operating in an overexpanded state. In the interest of uncovering the viscous mechanisms driving shock-induced separation resulting from overexpansion, an experimental investigation of an overexpanded system has been conducted and analyzed in conjunction with numerical and analytical results.

3.1 Supersonic Nozzle

The nozzle possessed by Embry-Riddle Aeronautical University is shown in Fig. 3.1. It is a 2-D (planar), asymmetric de Laval nozzle, with a maximum area ratio corresponding to a Mach number of 2.59. Nozzle geometry is defined in Table 3.1. The nozzle has a constant 1-inch thickness along the entire length of the nozzle and diffuser.

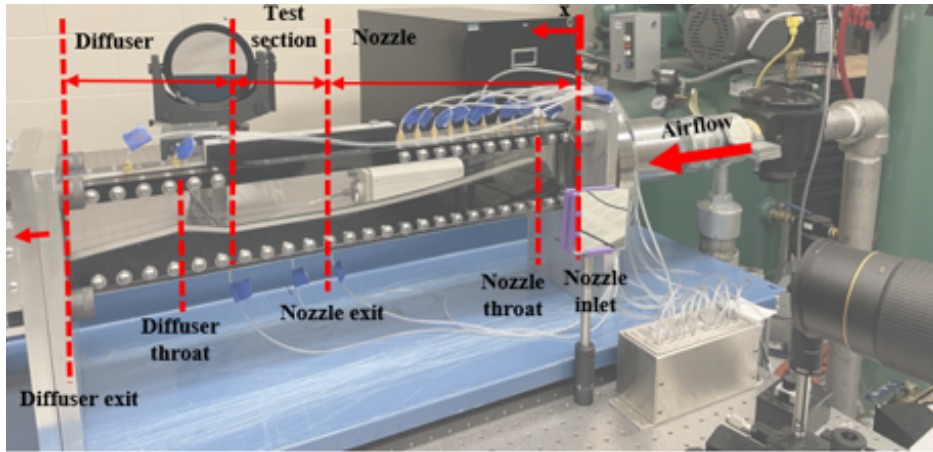


Figure 3.1 Supersonic nozzle.

Table 3.1 Nozzle geometry.

	Nozzle		Diffuser		Pressure Taps
A_e/A_1^*	2.868			L_1	2.6 in
M_e	2.59	A_d^*/A_1^*	2.2732	L_2	16.5 in
$L_{converging}$	2.432 in	$L_{diffuser}$	6.568 in	A_1	0.769 in ²
$L_{diverging}$	17 in			A_2	2.196 in ²
A_1^*	0.765 in ²				

3.2 Facility

The nozzle was installed in an intermittent open-loop blowdown-type wind tunnel facility, shown in Fig. 3.2. The defining characteristic of intermittent tunnels is the limit to run time due to a limited air supply. In a blowdown tunnel, the air is stored at high pressure in large tanks, and released through the tunnel and diffused out into the atmosphere, forming an open-loop system.

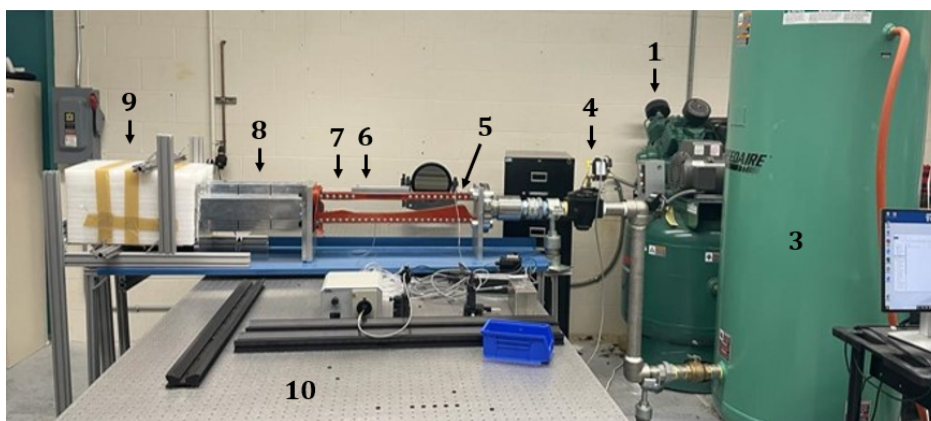


Figure 3.2 Experimental facility located in LB182B.

Details of the primary subassemblies of the blowdown tunnel are as follows:

1. **Compressor** (*Champion VR7F-8*): A two-stage piston compressor is used to pump air into the storage tank. The compressor power dictates the required rest interval between tunnel runs, as the system must be reinitialized after each run.
2. **Dryer** (*Quincy QMOD00035*): A high-pressure dryer is used to filter impurities and adsorb water vapor from the compressed air stream by collecting condensed air on the surfaces of a activated alumina desiccant.
3. **Air storage system** (*Grainger Speedaire 240 gal Air Tank*): A steel pressurized storage tank holds the stagnant compressed air before it is released through the tunnel. The maximum capacity of the tank is 240 gallons, with a maximum operating pressure of 200 psia.

4. **Pressure regulator** (*ProportionAir R000B*): A pressure regulator is installed to maintain a constant high pressure downstream of the pumping system. The R-series volume boosters are diaphragm operated, self-venting regulators.
5. **Nozzle** ($M = 2.59$): The nozzle accelerates the flow from subsonic to supersonic velocities. Details regarding the nozzle have been provided in Table 3.1.
6. **Test section**: Inside the nozzle assembly lies a short constant area section in which a model may be mounted. For the purposes of this study, the test section is left empty so that nozzle flow processes may be examined without any additional disturbances.
7. **Diffuser**: At the end of the nozzle assembly lies a diffuser through which the air is discharged. The diffuser is meant to slow the flow through a series of oblique shocks so that the flow exiting the system is not entirely supersonic, decreasing the jet noise and increasing safety.
8. **Silencer**: A silencer is used for acoustic control to reduce the noise levels generated by the tunnel before releasing the air into the atmosphere. The configuration developed for this facility consists of a straight rectangular channel with acoustic chambers on all four sides of the duct. Each chamber is filled with sound-absorbing material (Thermafiber mineral wool) and has a perforated channel facing the flow to protect the porous material from the airflow.
9. **Baffle**: An acoustic baffle enclosure is bolted down at the end of the tunnel to collect loose dampening material forced loose from the silencer and for further acoustic control. The baffle is filled with soundproofing foam panels, and the back end of the baffle is a mesh covering so that air may be exhausted from the system.
10. **Optical table** (*Newport Integrity 2 VCS system*): A rigid-leg pressurized optical table support system is used to provide broadband dampening of any disturbances to the

system through pneumatic isolators to ensure that all optical equipment is isolated from any vibrations introduced by the tunnel during runs.

3.3 Experimental Approach

Variances in nozzle flow resulting from changing upstream total pressure, and specifically characteristics of internal separation will be defined both qualitatively and quantitatively by visualizing the flow and measuring static wall pressure over a range of NPRs. From this data, separation shock strength can be defined, the location of the separation point can be monitored, and system performance can be quantified.

3.3.1 Experimental Setup

After the nozzle was installed in the blowdown tunnel, the nozzle was outfitted with pressure taps running along the length of the nozzle and test section to measure wall static pressure to quantify the strength and location of the separation. The taps are interfaced with a Scanivalve 16-channel DSA3217-PTP pressure scanner via 0.06" tubing. In addition to the pressure scanner, a Z-type schlieren is setup to focus around the region of separation in the nozzle to identify turbulent structures associated with separation and identify causes of pressure fluctuations and transient effects.

Measurements were carried out over a series of isolated, repeated runs at each NPR within the range of interest. The storage tank is filled to its maximum capacity, and the pressure regulator is set to the desired inlet total pressure. Upstream total pressures were selected within the overexpanded regime for this system between 40-80 psia. Multiple runs were conducted at each pressure level to ensure repeatability of results.

The pressure scanner is triggered to begin data collection using the DSALink4 program, and then the camera is triggered to begin schlieren imaging, immediately following which the release valve is engaged and the air is discharged through the tunnel. Runs are manually triggered and stopped when a suitable steady-state period has been maintained. The release valve is disengaged, the schlieren imaging is paused, and then the pressure collection is stopped. The gate valve is closed and the compressor is turned back on to fill the storage

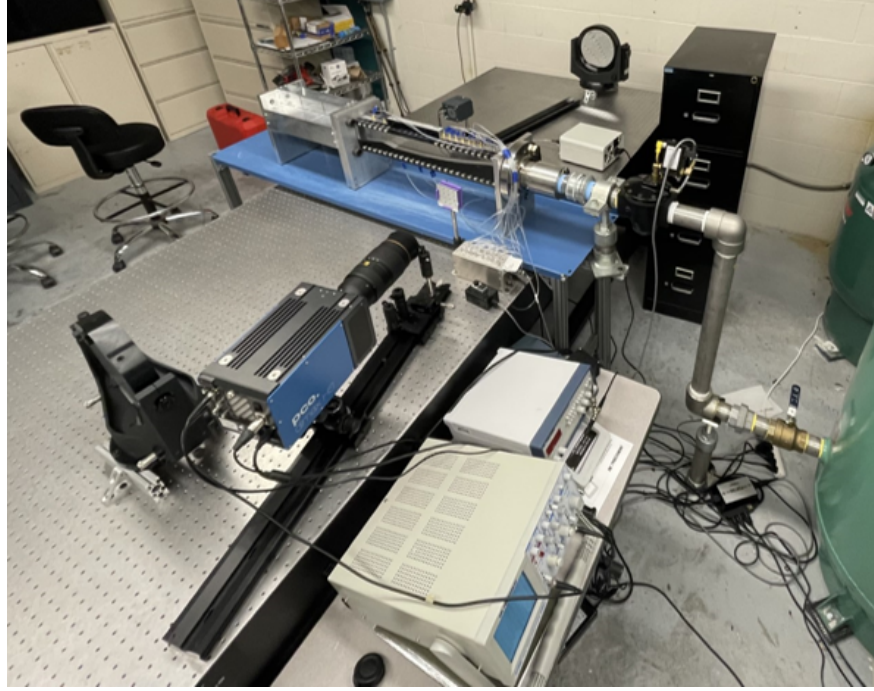


Figure 3.3 Experimental setup.

tank back up to its maximum capacity. Once this condition is reached, this process is repeated for all the total pressures of interest by adjusting the pressure regulator setting.

3.3.2 Schlieren Imaging

The flow within the nozzle and test section will be visualized using schlieren to identify any shocks or flow separation occurring within either component. Schlieren imaging is an optical technique for exhibiting any flow disturbances by projecting changes in fluid density by relying on light refraction as it passes through the working fluid [?]. A Z-type schlieren setup will be used, as shown in Fig. 3.5. In this setup, a light source emits a narrow beam of light that passes through the test section of the wind tunnel. The density variations in the flow cause corresponding changes in the refractive index, which in turn bend the light rays. [?]

A knife-edge or a razor blade is placed at the focal point of a lens, which focuses the light onto a high-speed camera. The knife-edge blocks the straight, undistorted rays, allowing only the bent rays to pass through. The refracted light forms a shadowgraph image on

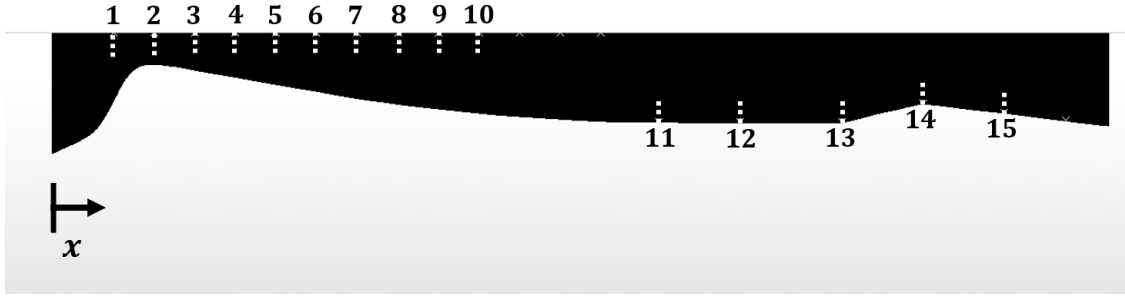


Figure 3.4 Pressure tap locations.

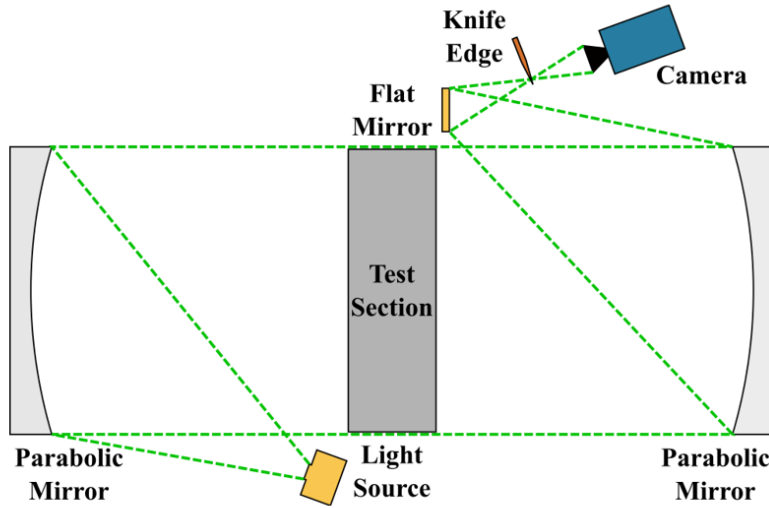


Figure 3.5 Z-type schlieren setup.

the screen or the camera, which reveals the density variations in the flow. Areas of higher density appear darker, while areas of lower density appear brighter. By carefully adjusting the position of the knife-edge and the focus of the lens, the system can be optimized to capture specific density gradients or shock waves in the supersonic flow.

In this particular setup, a PCO Dimax HS, a high-speed 12 bit CMOS camera, is used to capture schlieren images. A light source provided by University of Tennessee Space Institute is triggered synchronously with the camera. The light source is linked to the camera via a BK Precision 5 MHz signal generator and dual trace oscilloscope. Camera settings are adjusted to provide optimal spatial and temporal resolution for this system. A spatial resolution of 2000 by 1052 pixels and a frame rate of 4192 frames per second were used for imaging, with

a light source pulse width of 0.75 microseconds.

3.4 Experimental Results

Experimental results were conducted at the same upstream conditions as implemented computationally. Each test condition was performed multiple times to ensure repeatability of results. Pressure data was averaged over the steady-state time interval. This interval was set to be the length of time at which the maximum total pressure was supplied to the system. Total pressure is determined by applying isentropic relationships to the static pressure at a tap within the converging section of the nozzle, where losses are expected to be negligible. The area ratio of this tap location is used to inform the ratio of static to total pressure at this location:

$$p_0 = \frac{p_0}{p_1} * p_1 \quad (3.1)$$

Where p_1 is the static pressure at pressure tap 1, which has an area ratio of 2.18, corresponding to a pressure ratio p/p_0 of 0.9477. Nominal total pressure values were set using the pressure regulator, and the exact experimentally derived total pressures, although in fairly close agreement with setpoint values, were used to inform the boundary conditions for the computational analysis in the previous section. Attainable run times increased at lower upstream pressures, as expected. The maximum attainable run times are shown in Fig. 3.6. Pressure conditions were chosen to fall within the overexpanded regime while able to maintain a suitable steady-state test window.

Steady-state averaged pressure data allows for the pressure distribution across the stream-wise length of the nozzle to be extracted, as shown in Fig. 3.7. There is high static pressure at the nozzle inlet, which drops as the flow accelerates through the diverging section until the flow separates off of the nozzle wall. The static pressure increases over the separation shock, and continues to increase until it reaches the diffuser. The averaged pressure data indicates a separation location lying between 9.5 and 10.5 inches downstream of the inlet. When nondimensionalized by the appropriate total pressure, as shown in Fig. 3.8, the pres-

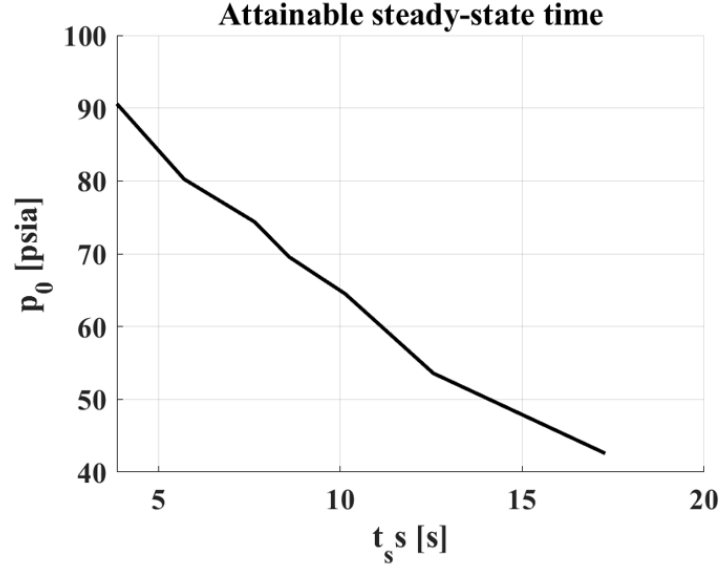


Figure 3.6 Attainable steady-state times.

sure curves prior to the separation are seen to coalesce, following the curve for isentropic expansion. Following the separation, lower pressure ratios are seen to have higher pressure ratios, representing a more severe level of overexpansion.

Schlieren imaging was conducted simultaneously with the pressure measurements. An image from the 76 psia test selected from the steady-state timeframe has been annotated here with key identifying features in Fig. 3.9. Unannotated images can be found in the Appendix.

Separation was observed at each of the selected total pressures. The strength of the separation shock is determined experimentally from the ratio of static pressure just after and before the shock, shown in Fig. 3.10. Increases in nozzle pressure ratio result in a general decrease in shock strength. As the NPR gets closer to the design value of 7.48, the severity of overexpansion decreases and the shock is not as strong. This explains the relatively higher attainable thrust capabilities at higher NPRs.

The pressure ratio across the shock quantifies the strength of this shock, and it can be seen that within the overexpanded regime, higher NPRs produce weaker shocks. It is clear that as upstream total pressure is reduced, the location of the separation moves upstream,

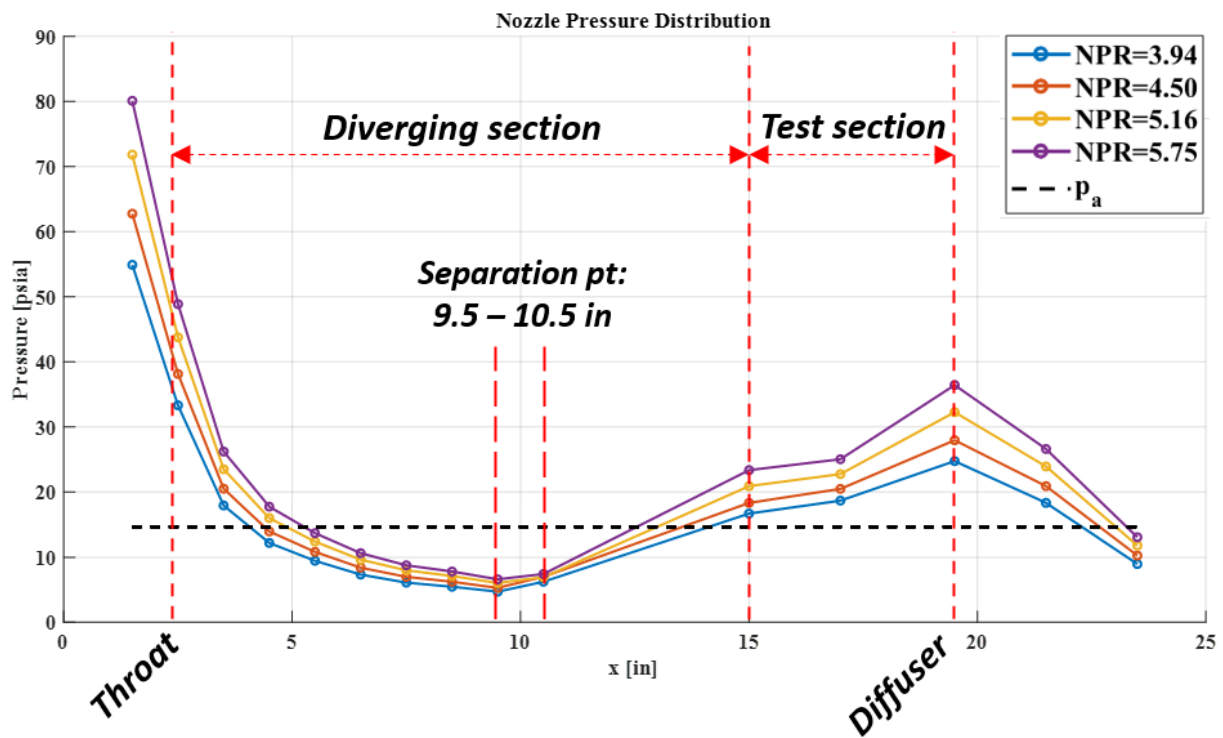


Figure 3.7 Pressure vs. position in nozzle, over NPR range.

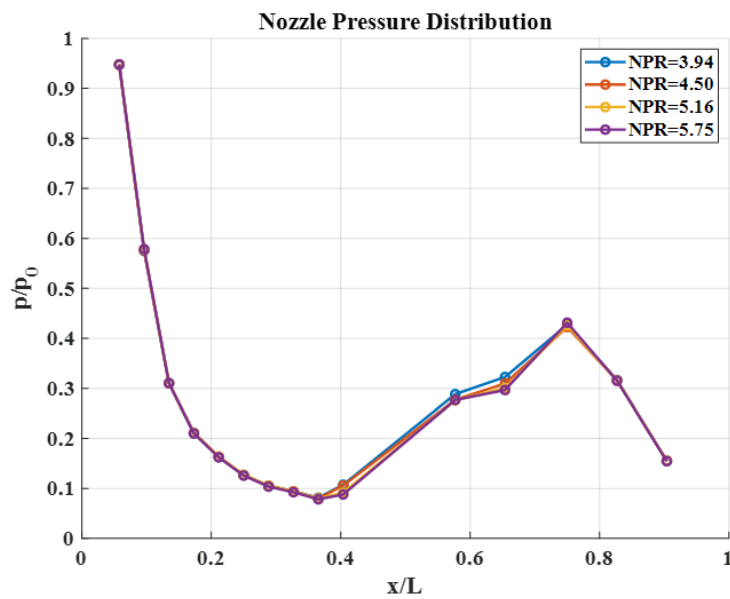


Figure 3.8 Pressure ratio vs. position in nozzle, over NPR range.

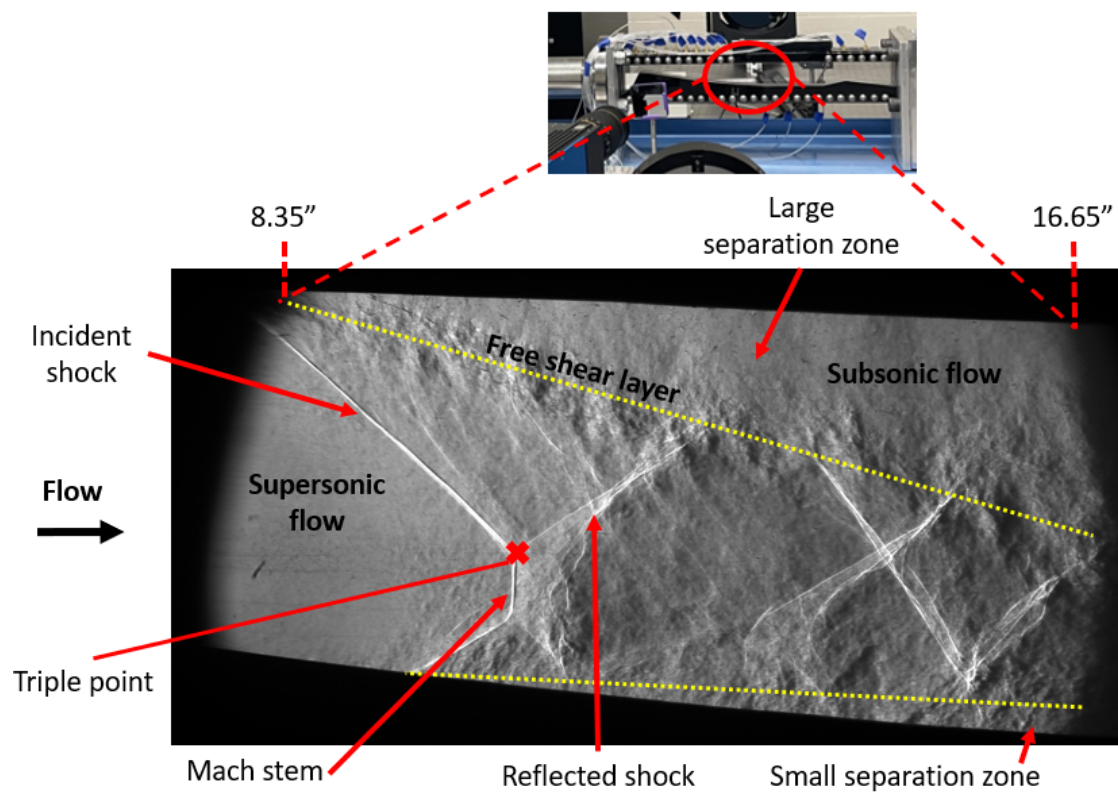


Figure 3.9 Schlieren of separation zone, $p_0 = 76$ psia.

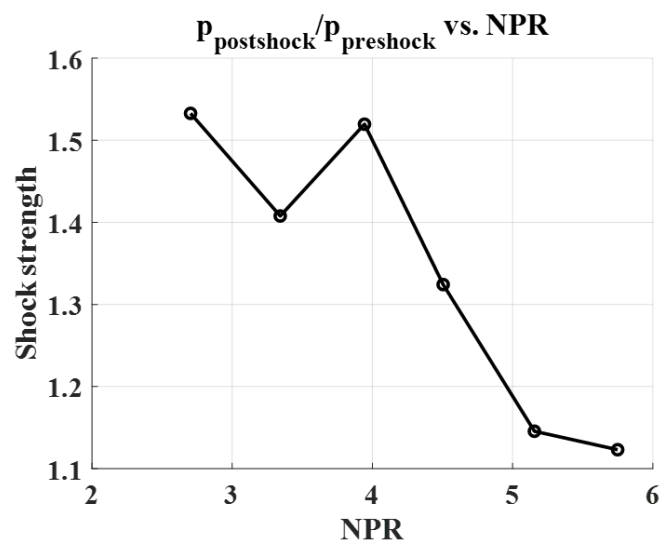


Figure 3.10 Separation shock strength vs. NPR.

Table 3.2 Location of separation shock

p_0 [psia]	NPR	Min x_{sep} [in]	Max x_{sep} [in]
75.78	5.155	8.64	10.08
66.21	4.504	8.06	9.78

as expected. Also at lower pressures, the Mach stem (normal portion of the separation shock structure) becomes more defined. The location of the separation is determined through both pressure data and schlieren, however it is seen that this location is not constant. Unlike the CFD, which seeks a mean steady-state solution, the experimental separation shock oscillates in the axial (streamwise) direction, even in the steady-state timeframe while constant supply conditions are supplied to the system.

Two cases in particular are studied to examine this oscillation, with NPRs of 4.50 and 5.16. Schlieren images of the maximum and minimum separation location for each case are shown in Fig. 3.11 and 3.12. The exact location of separation is obtained through scaling these schlieren images and determining the pixel to length ratio. These images can then be analyzed to extract the exact location of the separation, as shown in Fig 3.13. Resulting values are shown in Table 3.2. The separation locations are validated by the pressure data. Because the maximum downstream separation location is seen to fall within the steady-state interval in which the pressure increases, it can be concluded that this is not a steady oscillation, and the separation shock lies closer to the downstream location for a longer time period, which is validated through a compilation of schlieren images.

The silencer was added to the end of the nozzle to reduce audible noise levels in the building during testing. In order to confirm that the silencer did not induce a change in back pressure on the nozzle and therefore alter any obtained results, tests were performed with the silencer both on and off. Results yielded identical data between both cases, confirming the lack of interference, as shown in Fig. 3.14 and 3.15.

The final parameter extracted from the collected data is the thrust and thrust coefficient, using the analytical method described by Papamoushou [?], explained in Chapter 2. The

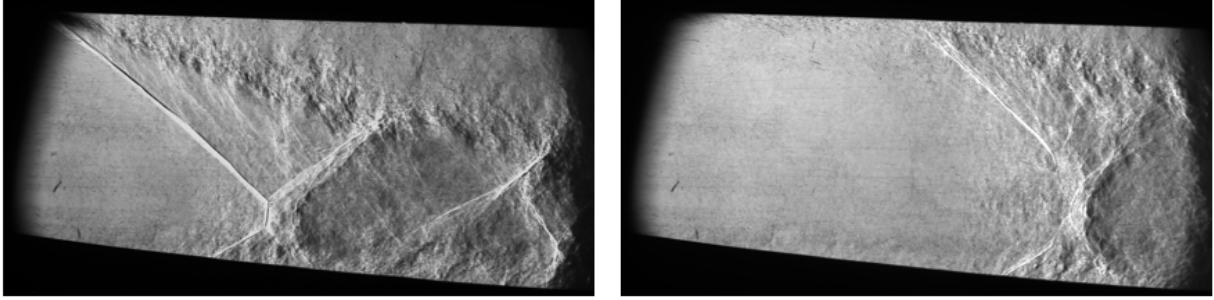


Figure 3.11 Schlieren, variation in separation location at $NPR = 4.50$.

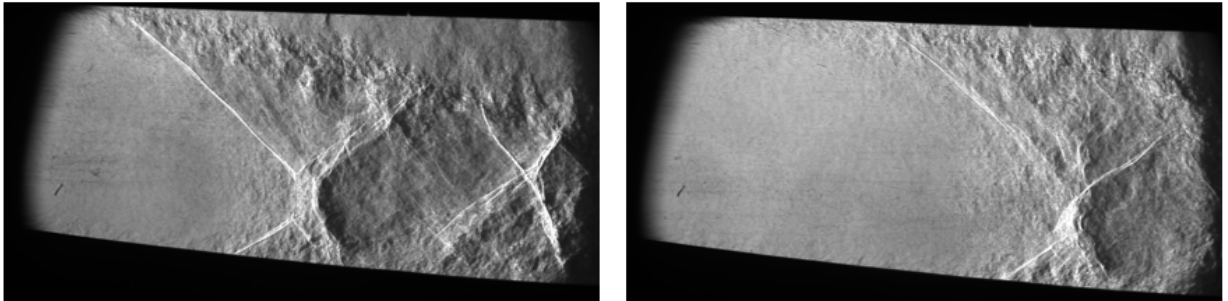


Figure 3.12 Schlieren, variation in separation location at $NPR = 5.16$.

results of integrating the pressure distribution are shown in Fig. 3.16 and 3.17, for each NPR as compared to the ideal thrust obtained from the design condition.

A reduction in nozzle performance is seen at off-design conditions as opposed to the ideal design case, quantified via the thrust force and coefficient calculated analytically from the pressure distribution. Overexpansion resulted in a 5.2% reduction in thrust at $NPR = 5.75$, and a 15.3% reduction in thrust at $NPR = 2.70$. This thrust estimate does not include shear stresses, since their impact is much smaller than the pressure distribution created by the shock. Lower NPRs represent more severe overexpansion, which as seen earlier, is associated with stronger separation shocks, leading to a higher total pressure loss, and thus a decreased attainable thrust. The overall trends and values obtained here are consistent with direct thrust measurements of past works in nozzles of similar scales [?].

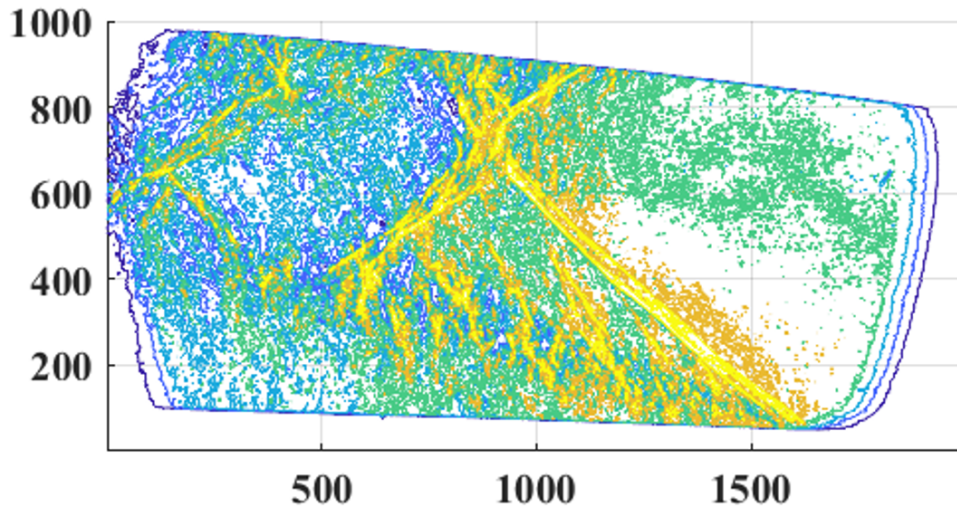


Figure 3.13 Schlieren scaling.

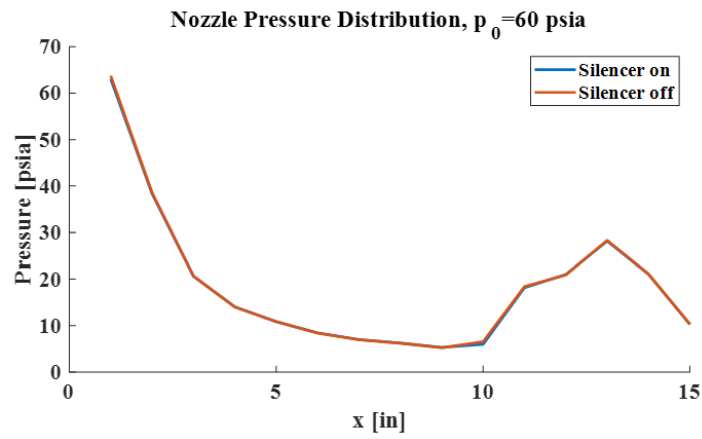


Figure 3.14 Pressure distribution with silencer on and off, $p_0 = 66$ psia.

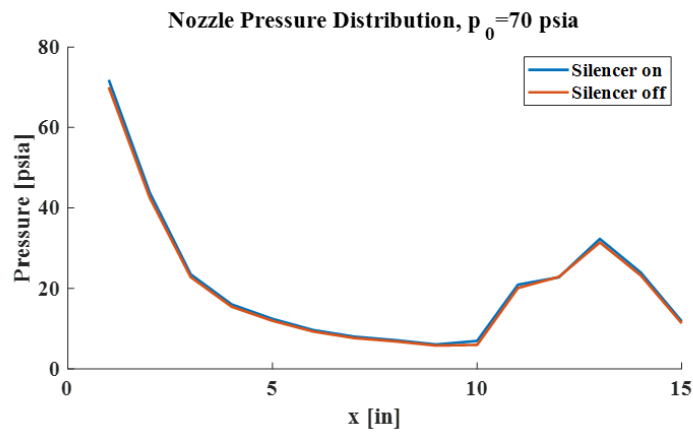


Figure 3.15 Pressure distribution with silencer on and off, $p_0 = 76$ psia.

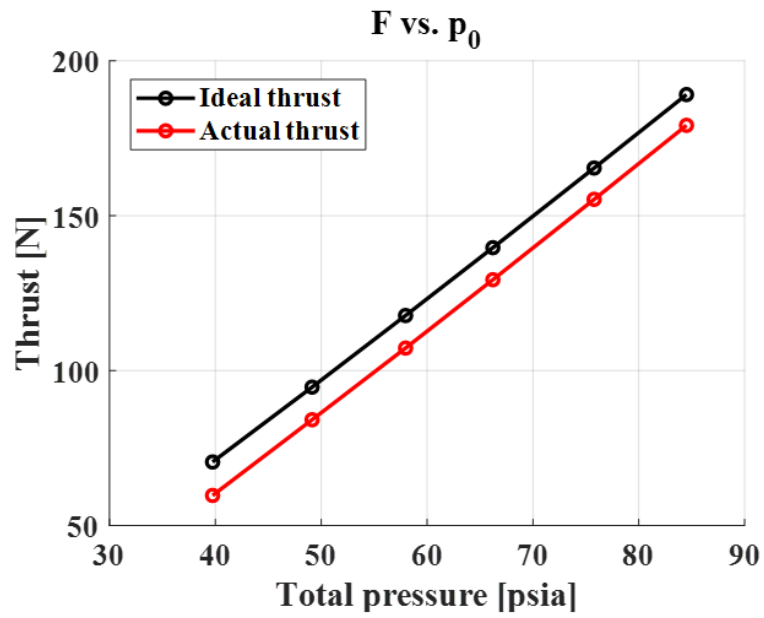


Figure 3.16 Thrust vs. NPR.

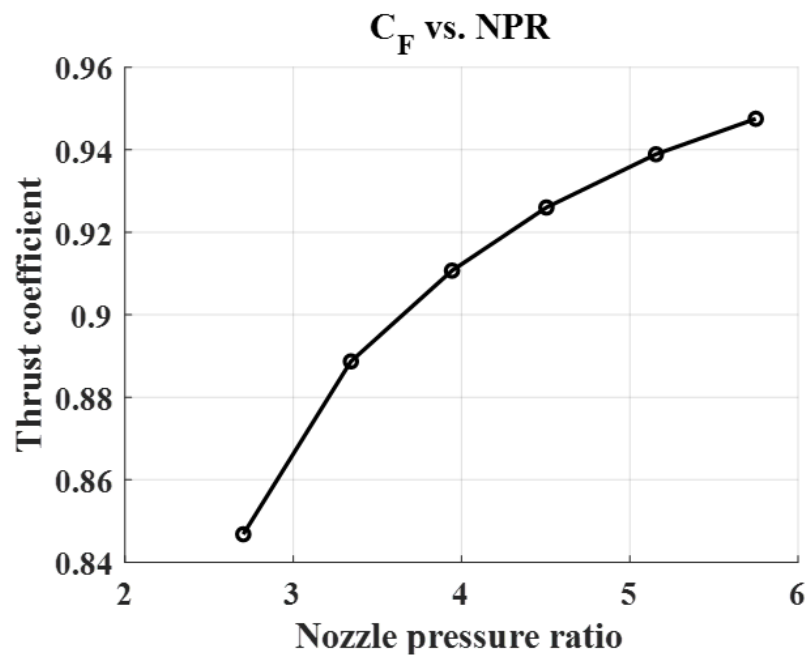


Figure 3.17 Thrust Coefficient vs. NPR.

3.5 Modeling Nozzle Geometry

It was desired to predict the effects of overexpansion due to reduced upstream total pressure on nozzle performance with computational fluid dynamics (CFD) simulations, so that analytical, numerical, and experimental results could be compared. There was no previous documentation of nozzle geometry or design practices, so in order to perform computational simulations, an accurate model of nozzle geometry had to be generated. This was accomplished using an Einscan 2x Pro 3-D scanner employing LIDAR technology to scan the nozzle. The scan produced a point cloud used to generate a fine mesh, from which the nozzle contour could be extracted exactly and developed into a solid model. This scan was also used to pinpoint the exact locations of the pressure taps located on the top and bottom of the nozzle. Raw scan results and the resulting solid geometry of the flow channel are shown in Fig. 3.18 [?].

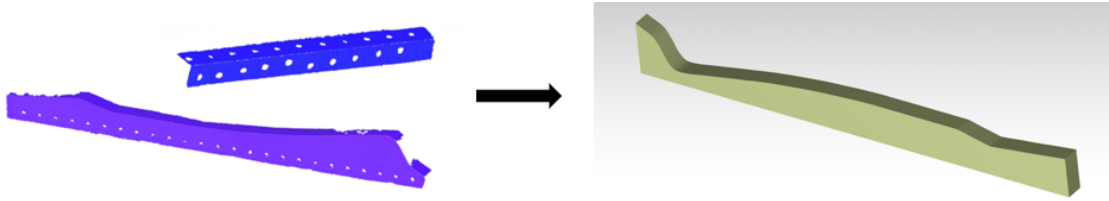


Figure 3.18 3-D scan output and resulting nozzle geometry.

3.6 Computational Approach

Computational results were obtained in Ansys Fluent using an implicit density-based AUSM formulation with a 2nd order k-omega SST turbulence model. Mesh and CFD parameters are given in Table 3.3. The mesh is largely unstructures, with T-rex quads near the walls to resolve the boundary layer. The whole mesh is shown in Fig. 3.19, and the clustering around the throat region is shown in Fig. 3.20.

3.7 Design Condition

The ratio of the maximum to minimum (throat) areas of the nozzle defines the expected performance and required conditions for perfect expansion through the nozzle. The ratio

Table 3.3 CFD Solver Parameters

Boundary conditions	Total pressure inlet: Changed based on case of interest
	Static pressure outlet: 14.7 psia (atmospheric)
	Wall: Nozzle internal surfaces
Submodels	Viscous model: k-omega SST
Numerical Scheme	AUSM
Spatial Discretization	Turbulent kinetic energy, specific dissipation rate: Second Order Upwind
Cell count	74,741
Maximum $y+$	4.71

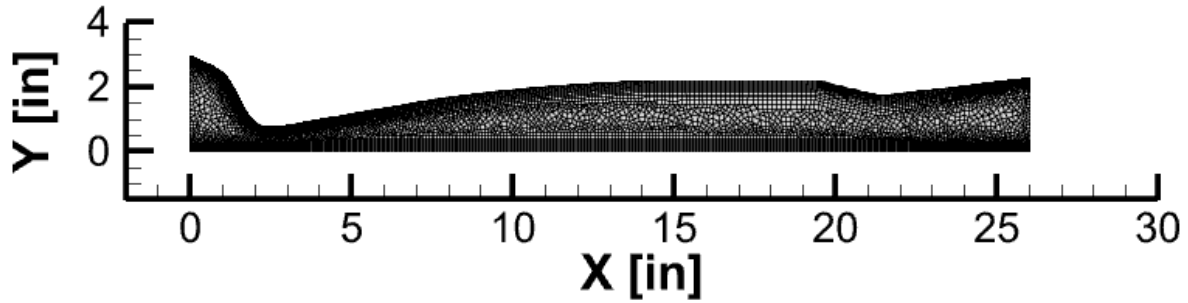


Figure 3.19 Nozzle mesh.

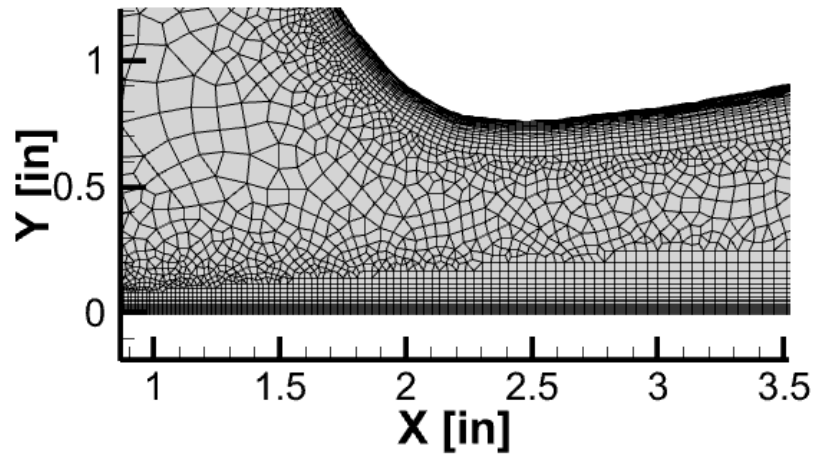


Figure 3.20 Nozzle mesh around throat.

of expected exit plane conditions to total conditions were obtained 1-D isentropic relations. Maximum velocity occurs at the nozzle exit plane, corresponding to the largest area ratio. Nozzle isentropic parameters are provided in Table 3.4.

The nozzle expansion case is defined by the ratio of the exit plane static pressure to the ambient (back) pressure in which the nozzle is exhausted, in this case, ambient pressure. The design condition is defined by the required total upstream pressure so that the nozzle exit pressure is equal to the ambient pressure, and so the isentropic exit Mach number is reached. Once the flow has properly expanded through the nozzle, further increasing the total pressure will not increase test section Mach number, which is a function of nozzle geometry only, rather it will increase static pressure and subsequently the flow will undergo relatively smaller losses as it is ejected through the diffuser. Thus, there is a certain upstream pressure, defined to be the design pressure of 110 *psia*, at which the flow will expand isentropically through the nozzle and reach a minimum exit pressure from the diffuser. This design value was validated numerically by iterating upstream pressure until this condition was met, and thus ideal flow at design conditions was simulated. Corresponding total temperature and density are determined from ambient conditions and equation of state to be 300 *K* and 8.81 *kg/m³*.

3.7.1 Numerical and Analytical Results

The numerical results displays good agreement with expected values, exhibiting an expansion up to Mach 2.549 with minimal total pressure losses, visible in the contours of Mach number and static pressure shown in Fig. 3.21. Comparison of analytical isentropic results and computational results taken from the are-weighted average over the nozzle exit plane are tabulated in Table 3.4. System performance can be classified as adiabatic, but not entirely isentropic, as losses in total pressure are evident, causing lower numerical exit plane static pressures than predicted isentropically. Results do indicate a somewhat inefficient diffuser design, as the flow is not completely decelerated to the subsonic regime before being ejected from the system. This result validates our solid model, so that off-design conditions may be

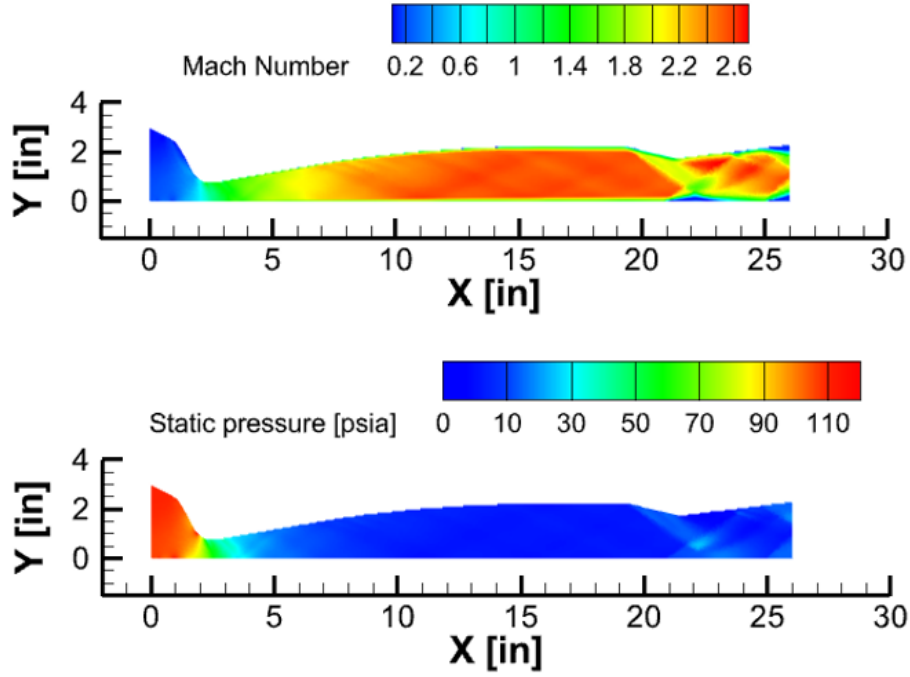


Figure 3.21 Contours of a) Mach number and b) static pressure, design condition ($p_0 = 110$ psia.)

accurately reproduced and compared to experimental data.

3.8 Overexpanded Condition

The experimental results will be obtained with the nozzle operating in the overexpanded regime to analyze the viscous effects driving this phenomenon and the resulting turbulent structures and effects on nozzle performance. The overexpanded condition is the primary case of interest and effects will be quantified and compared to those obtained analytically and numerically under the design condition. The upstream total pressure will be altered to induce a range of NPRs and therefore levels of severity of overexpansion. Multiple cases will be run ranging from 40-80 psia. The highest pressure will be studied first, and then the chamber pressure will be reduced trial by trial until results have been obtained for all cases.

Table 3.4 Numerical and Isentropic Nozzle Exit Plane Parameters (Design condition, $p_{0inlet} = 110 \text{ psia}$)

		$p_{0inlet} = 110 \text{ psia}$		$p_{0inlet} = 76 \text{ psia}$		$p_{0inlet} = 66 \text{ psia}$	
		Isentropic expectation	Exit plane	Pre-separation	Exit plane	Pre-separation	Exit plane
p_0	(psia)	110	97.76	75.78	30.11	66.21	38.70
M_e		2.590	2.549	2.56	0.8676	2.56	1.4361
p_e/p_0		0.0509	0.0625	0.0495	0.5098	0.0543	0.2817
p_e	(psia)	5.599	6.1104	3.75	15.35	3.60	10.90
T_e	(K)	128.1	130.74	130.77	250.38	134.37	203.18
T_0	(K)	300	299.95	299.91	292.96	299.95	293.07
T_e/T_0		0.427	0.4357	0.4360	0.8546	0.4480	0.6933
ρ_e	(kg/m ³)	0.659	1.1221	0.6731	1.5020	0.6407	0.9954
u_e	(m/s)	587.53	583.83	586.69	266.65	580.59	382.59
a_e	(m/s)	226.87	229.04	228.20	316.46	228.29	283.72

Table 3.5 Comparison of Numerical and Experimental Shock Characteristics

	66 psia		76 psia	
	CFD	Experiment	CFD	Experiment
Shock strength	2.045	1.324	1.956	1.146
Shock location [in]	11.69	8.06 - 9.78	14.20	8.64 - 10.08

3.8.1 Numerical Results

Computations were performed using the same CFD solver parameters as the design condition and converged to a steady-state solution. Contours of Mach number and pressure are shown for each upstream pressure in Fig. 3.22 and 3.23. The results clearly exhibit shock-induced separation occurring as a result of overexpansion. A sharp decrease in Mach number and increase in static pressure occur over the separation shock. The pressure ratio over the shock, as well as the location of separation downstream of the inlet, are tabulated and compared to experimental results in Table 3.5. Computational results displayed a clear separation shock associated with internal separation, however the characteristics of this separation were not able to be predicted with accuracy. The shock strength was overpredicted computationally, and the location of separation was also seen to be further downstream than observed experimentally.

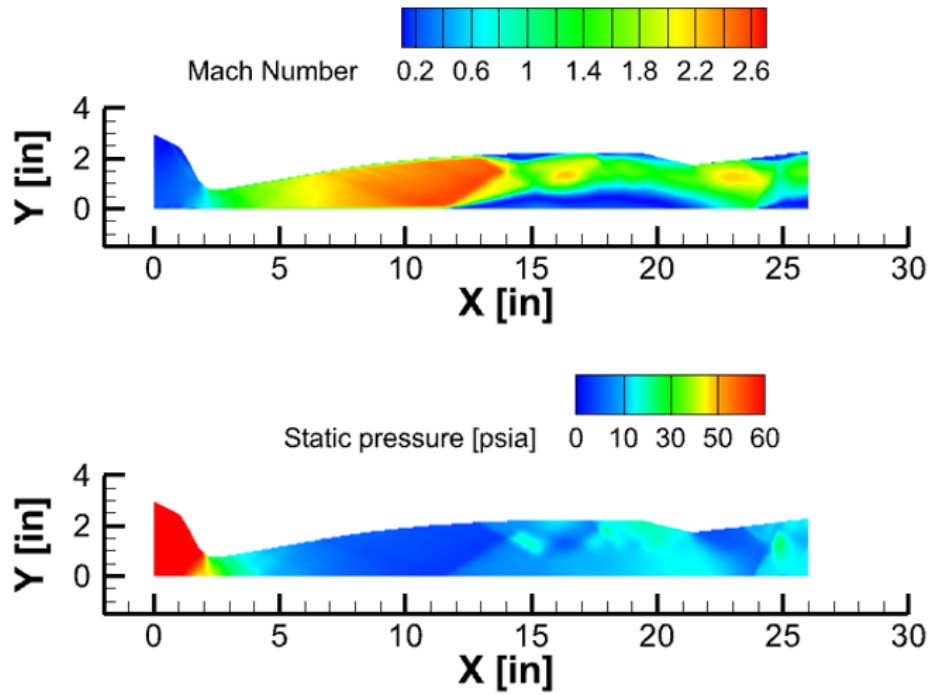


Figure 3.22 Contours of Mach number and static pressure, $p_0 = 66$ psia.

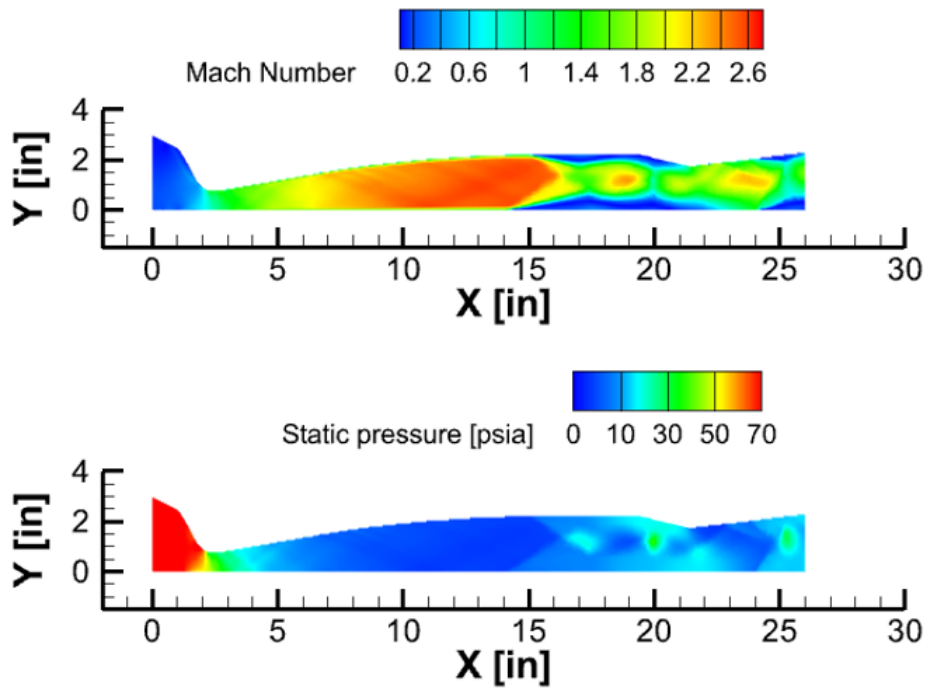


Figure 3.23 Contours of Mach number and static pressure, $p_0 = 76$ psia.

4 Nozzle Design

The second facet of the project was a complete design phase for the de Laval nozzles to be implemented into the SWT facility. The primary components of the wind tunnel include interchangeable de Laval nozzles designed to provide the necessary conditions to replicate supersonic flow at Mach numbers of 2 and 3. These components have been designed and simulated to ensure Mach number uniformity and will be fabricated in house out of Aluminum 6061.

Designing a supersonic wind tunnel nozzle requires maintaining a clean and uniform flow at the exit where the nozzle joins the test section by limiting the strength of shocks within the nozzle. Maintaining such conditions can be challenging and requires better contour design criteria and numerical simulations to back these designs before fabricating them for installation in the wind tunnel. As discussed in Chapter 2, a typical algorithm for such a design is the method of characteristics (MOC), which utilizes the compatibility equations for the supersonic portion of the nozzle [? ?]. MOC has been successful in designing both rocket nozzles [?] optimized for maximum thrust, and wind tunnel nozzles [?] optimized for uniform flow properties. Hence, it is important to define design requirements and desired flow characteristics when utilizing MOC [?].

It is possible to obtain successful nozzle designs without considering viscous effects; in previous studies, inviscid nozzle design has shown concurrence with CFD analysis [?]. However, boundary layer growth does have an impact on the attainable region of uniformity within the test section, as excessive boundary layer growth may lead to detachment from tunnel surfaces, disrupting the centerline flow. Unless at low stagnation pressures, the boundary layer is typically assumed to be turbulent in supersonic wind tunnels. Thus, it is beneficial to correct nozzle designs for boundary layer growth to obtain a wider region of uniform core flow in the test section.

The primary objective for the current work is to design and numerically validate interchangeable nozzles of same length for use in a supersonic blowdown-type wind tunnel facility.

The nozzles designed in the current study are intended to produce Mach 2 and 3 flow, with provisions for potential Mach 4 use. The design parameters are laid out and both inviscid design and viscous correction to the designs will be discussed. This work will explore design of both the convergent (subsonic) and divergent (supersonic) portion of the nozzles. A detailed two- and three- dimensional CFD analysis will then be carried out on all the nozzles to ensure flow regularity and quantify the three-dimensional effects such as corner vortices and sidewall interaction on the variation of test section parameters, with the ultimate goal of limiting these variations as much as possible.

The nozzles are to be interchangeable so that nozzles designed for different test section velocities could be removed and added depending on the desired test conditions, and so constant inlet and length dimensions are required. The first nozzle developed was designed for operation nominally at Mach 2, and subsequently, a Mach 3 nozzle was developed. The test section must be shock-free with dimensions 4"x4"x15", with uniform free-stream velocity and optical access. Finally, a run time of at least one minute was desired, which is dictated by the attainable system stagnation pressure, or the capacity of the tanks which the air is stored.

4.0.1 Sivells' Method

As discussed in Chapter 2, the method of characteristics (MOC) is the algorithm typically used for designing the divergent portion of supersonic nozzles. Characteristic lines are defined as lines along which the derivatives of flow properties are indeterminate, and across which may be discontinuous. Along the characteristic lines, partial differential conservation equations can be combined in a way that ordinary differential equations are obtained, which are called compatibility equations. MOC consists of solving the compatibility equations step-by-step along the characteristic lines starting from the given initial conditions at some point or region in the flow. In this manner, the complete flow field can be mapped out along the general characteristics, and in the context of nozzle design, a contour can be obtained[?].

The code developed by J.C. Sivells utilizes MOC algorithms to generate ideal nozzle contours for supersonic and hypersonic wind tunnels based on provided input parameters [?], [?]. In Sivells' approach, the axial velocity distribution is divided into three parts as illustrated in Fig. 4.1. In the initial region, from sonic point I to point E, the velocity distribution is characterized by a fourth-degree polynomial. In the intermediate section, from point E to point B, radial flow is assumed, taking place within the boundaries of characteristics EG and AB. Here, the contour from point G to point A forms a straight line at an angle ω relative to the axis. From flow separation considerations, ω is usually no more than 15° and a common value for many nozzles is 12° . Lastly, the Mach number distribution from point B to point C is described by a fifth-degree polynomial, and beyond point C, uniform flow is assumed. The coefficients of these polynomials are selected to ensure the continuity of the second derivative of axial velocity throughout the nozzle, with the condition of being zero at point C. Two characteristic solutions are needed: one for determining the throat contour from point H to point G, and the other for establishing the downstream contour from point A to point D, representing the theoretical end of the nozzle, with the characteristic CD being a straight line defining the onset of the uniform flow region. [?]

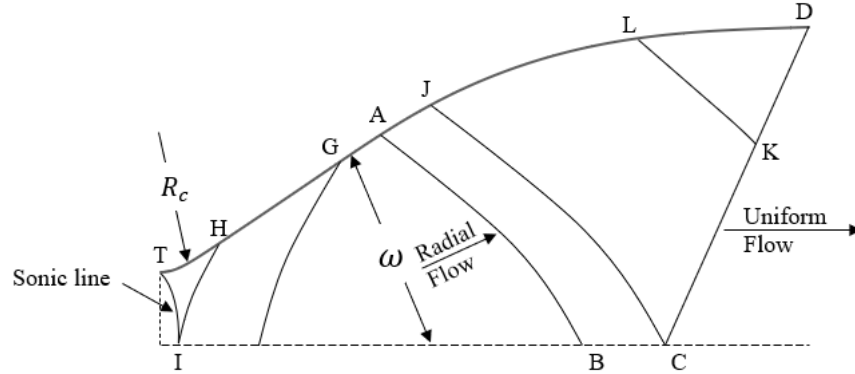


Figure 4.1 Regions of inviscid contour.

Sivells' method relies on an initial estimation of the nozzle expansion angle and throat radius of curvature for a specified design Mach number, denoted as Mach at point C. The Mach number at point B is assumed to be 90 percent of the design Mach number. Using these

initial inputs, Sivells' FORTRAN code can be used iteratively to calculate an estimated value for throat height, and consequently, nozzle area ratio, at specified stagnation conditions. The result is a viscous nozzle contour that has been corrected for some boundary layer development, however, the code's applied correction for boundary layer growth is greater than the displacement thickness on the contoured walls, which causes the flow to diverge in the test section[?]. Since the quality of flow in the test section is the main interest of wind tunnel nozzle design, Sivells' method requires additional corrections to properly accommodate boundary layer growth. First, a correction in Mach number is required to obtain the nozzle's 2-D inviscid contour for the previously obtained area ratio. Then, to account for turbulent boundary layer development in the flow, 1-D theory is applied to estimate the flow's displacement thickness, δ^* . See Eq. 4.1.

$$\delta^* = y_{e_{desired}} - y_s \cdot (A/A^*)_{1-D} \quad (4.1)$$

Where $y_{e_{desired}}$ represents the desired exit height, y_s represents the throat height, and $(A/A^*)_{1-D}$ is the area ratio for design Mach number with $\gamma = 1.4$ - not the corrected area ratio obtained from Sivells' code. For a more accurate design, the displacement thickness in the middle of the test section can be verified through CFD simulations. The correction for boundary layer growth is made by calculating the corrected throat height and its corresponding area ratio for a desired exit height. This can be done by calculating the inviscid height through Eq. 4.2.

$$y_{inviscid} = y_{e_{desired}} - 2 \cdot \delta^* \quad (4.2)$$

And subsequently the corrected throat height using Eq. 4.3.

$$y_{s_{corrected}} = y_{inviscid} / (A/A^*)_{1-D} \quad (4.3)$$

The contour needs to be corrected for an area ratio such that Eq. 4.4 is satisfied.

$$(A/A^*)_{3-D} = y_{e_{desired}}/y_{s_{corrected}} \quad (4.4)$$

This correction will be translated as an increase in Mach number and nozzle length. Once completed, the final 3-D physical contour is obtained for the divergent section.

4.0.2 Hopkins-Hill Method

The convergent section of the nozzle will be designed using the Hopkins-Hill method [?]. In their research, D. F. Hopkins and D. E. Hill developed a method to predict transonic flow features in nozzles with nearly sharp wall curvatures. The approach relies on a reference boundary designed to closely emulate the actual physical boundary of the nozzle. This reference boundary is mathematically expressed through an analytical function that ensures continuity in all derivatives. Serving as an initial approximation, the reference boundary is subject to iterative adjustments, refining its shape to better match the actual nozzle boundary in the throat region. The boundary's shape is modeled as a probability curve, determined by two parameters: C_1 and R_s . See Eq. 4.5.[?]

$$Y = C_1[1 - \exp(-x^2/2R_sC_1)] + y_s \quad (4.5)$$

The parameter R_s sets the throat's radius of curvature, while C_1 determines the entrance angle. Varying these parameters creates a family of curves, some depicted in Fig. 4.2.

Normalizing distances by throat height, y_s , introduces the parameter H_r , representing the reference boundary's contour in terms of C_1 and R_s (see Eq. 4.6).

$$H_r = C_1[1 - \exp(-\xi^2/2R_sC_1)] + 1 \quad (4.6)$$

Where ξ is the normalized distance in the x-axis. The first x-point of the distribution curve on the centerline axis, ξ_1 is obtained from R_s and the inlet's entrance angle θ_{sub} . See Eq. 4.7 below.

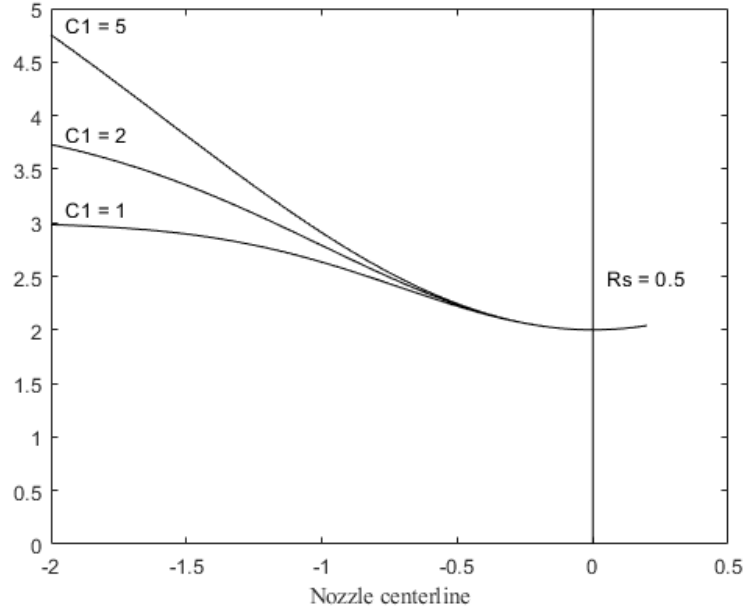


Figure 4.2 Reference boundary shape.

$$\xi_1 = -R_s \tan(\theta_{sub}) \exp^{0.5} \quad (4.7)$$

The value of C_1 can be calculated using Eq. 4.8.

$$C_1 = \xi_1^2 / R_s \quad (4.8)$$

The subsequent ξ -points along the distribution curve are computed based on the distance between ξ and the throat, where $\xi = 0$, and the desired number of points, denoted as n_{pts} . This parameter influences the slope of the contour. The x-axis distribution is expressed by Eq. 4.9 below.

$$\xi_{n+1} = \xi_1 + n \cdot dx \quad (4.9)$$

Here, dx is determined by Eq. 4.10, given by:

$$dx = \xi_1 / n_{pts} \quad (4.10)$$

In this fashion, as n approaches n_{pts} , the reference boundary aligns with the throat at $\xi = 0$, resulting in $H_r = 1$ with $y = y_s$. For an entrance angle of 45 degrees, this method establishes a ramp contour for the convergent section of the nozzle, which is critical for length considerations. From transitional Re_x , a minimum length can be calculated so that turbulent flow can be effectively induced into the throat. See Eq. 4.11.

$$L_{min} = Re_x \cdot \nu / U \quad (4.11)$$

This design adjustment is crucial for achieving the intended flow characteristics of the nozzle. The inlet can be curve fitted to a circular form at a desired height provided that the contour's slope remains relatively constant.

4.1 Nozzle Design Criteria

The nozzles to be designed are nozzles of different operating design Mach numbers, to be used interchangeably in a supersonic blow-down type facility without altering the relative location of the wind tunnel test section. This means that they will all have to be of the same nominal length. The three operating Mach numbers desired are Mach 2, 3 and 4. Hence, Mach 4 nozzle contour was used as the main length determining criteria.

The blowdown tunnel is planned to have a square test section of cross-section of 4-by-4 inch which sets the half-height of the nozzle at 2 inches. Table 4.1 mentions additional operating parameters set for the nozzle design. According to preliminary analysis of Mach 4 nozzle, the total length of all the nozzles was determined to be 24 inches.

4.2 Nozzle Contours

The final contours obtained as a result of this design process are shown in Figs. 4.3 and 4.4 for the Mach 2 and 3 nozzles, respectively.

4.3 Computational Results

Computational results were obtained in ANSYS Fluent using an implicit density-based AUSM formulation with a 2nd order k-omega SST turbulence model. Mesh and CFD pa-

Table 4.1 Nozzle Design Parameters

Nozzle 1	Uniform Mach 2 flowfield at nozzle exit Dry air supply at P_0 of 35 - 55 psiA and T_0 of 530R
Nozzle 2	Uniform Mach 3 flowfield at nozzle exit Dry air supply at P_0 of 80 - 120 psiA and T_0 of 530R
Inlet Geometry	4in \times 4in
Exit Geometry	4in \times 4in
Wall Type	Parallel walls
Additional Features	All nozzles will have common inlet and exits All nozzles will have the same length

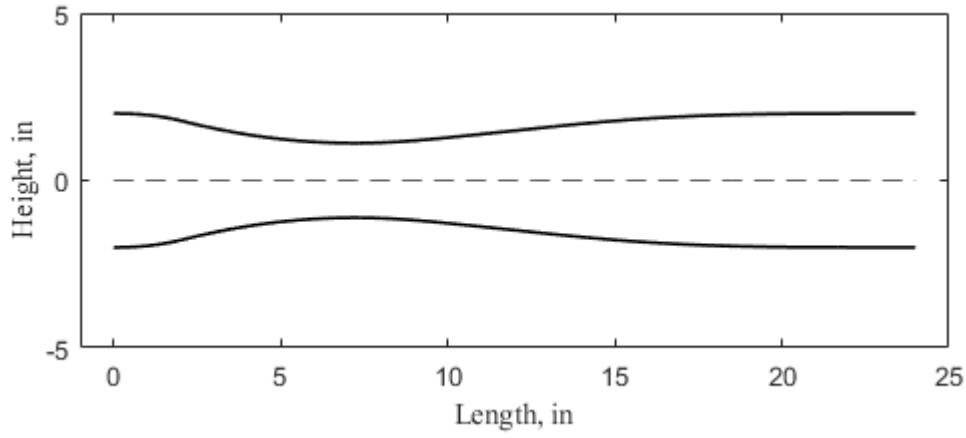


Figure 4.3 Mach 2 nozzle contour.

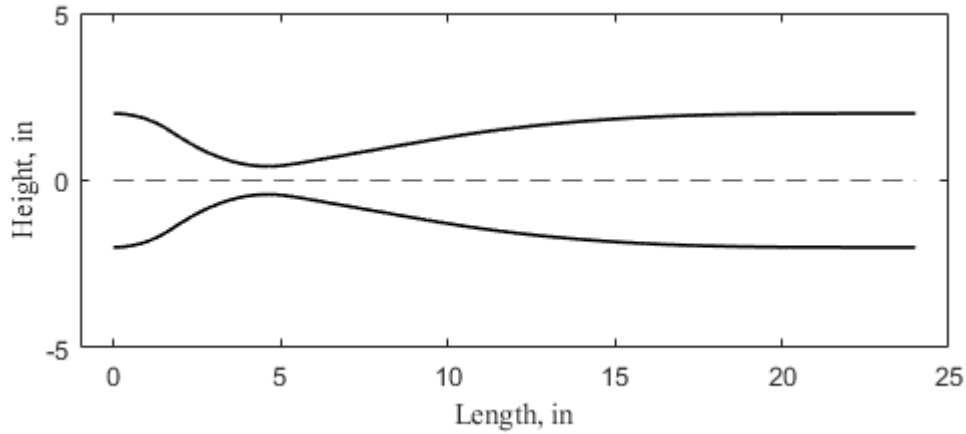


Figure 4.4 Mach 3 nozzle contour.

rameters are given in Table 4.2. The flow channel includes the 2-D nozzle, as well as a 15 inch test section added to examine the streamwise variation in Mach number as the boundary layer thickens through this region. The structured mesh generated for these nozzles are shown in Fig 4.5 and 4.6. The mesh for these components has been resolved through the boundary layer across the entire nozzle length.

Table 4.2 CFD Solver Parameters

Boundary conditions	Total pressure inlet: Mach 2: 45 psia Mach 3: 100 psia
	Static pressure outlet: $p_b = p_e$ (perfectly expanded)
	Wall: Nozzle internal surfaces
Submodels	Viscous model: k-omega SST
Numerical Scheme	AUSM
Spatial Discretization	Turbulent kinetic energy, specific dissipation rate: Second order upwind
Cell count	Mach 2: 470,596 Mach3: 475,398
Maximum $y+$	Mach 2: 1.86 Mach 3: 4.61

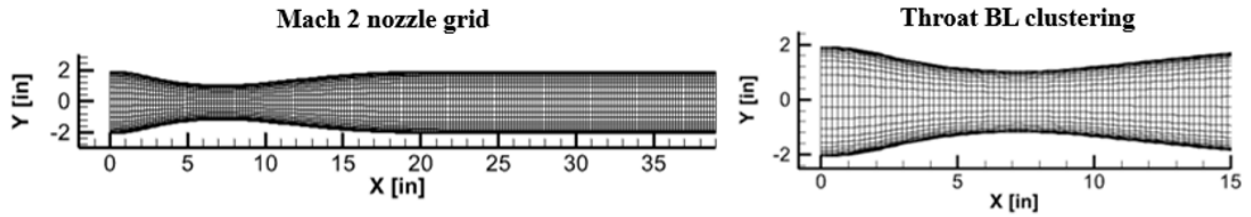


Figure 4.5 Mesh for Mach 2 nozzle.

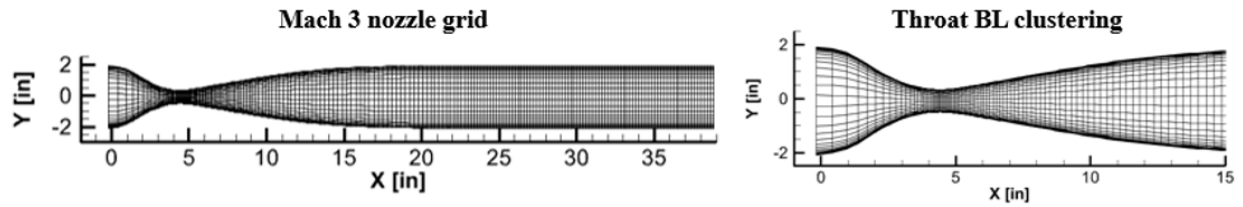


Figure 4.6 Mesh for Mach 3 nozzle.

First, two-dimensional analysis was performed on the nozzles for preliminary design verification. The CFD results show that the exit plane contains a very limited velocity gradient, in alignment with the nozzle design objectives. However, due to the constraint of parallel test section walls for this system, there is some weak shock that forms in the interface between the nozzle and the test section, since the unaltered flow wants to keep expanding but is in turn limited by the test section walls. This density gradient is not intense and will be accounted for in tunnel calibration and characterization. The numerical results displays good agreement with expected values, exhibiting an expansion up to Mach 2.034 and 3.043 with minimal total pressure losses, visible in the contours of Mach number shown in Figs. 4.7 and 4.8 respectively. Comparison of analytical isentropic results and computational results taken from the area-weighted average over the nozzle exit plane are tabulated in Table 4.3.

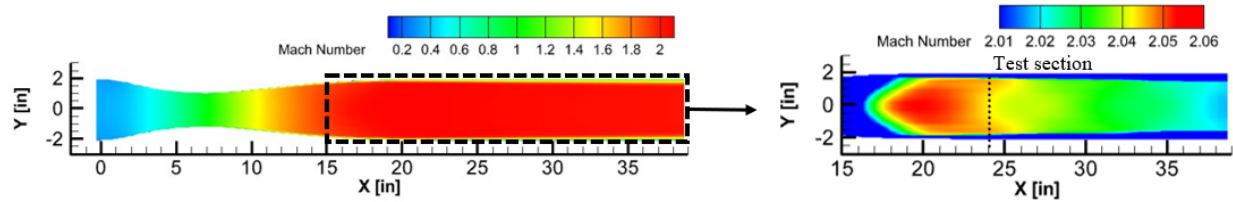


Figure 4.7 Contours of Mach number in Mach 2 nozzle through a) entire channel, b) test section ($p_0 = 45 \text{ psia}$).

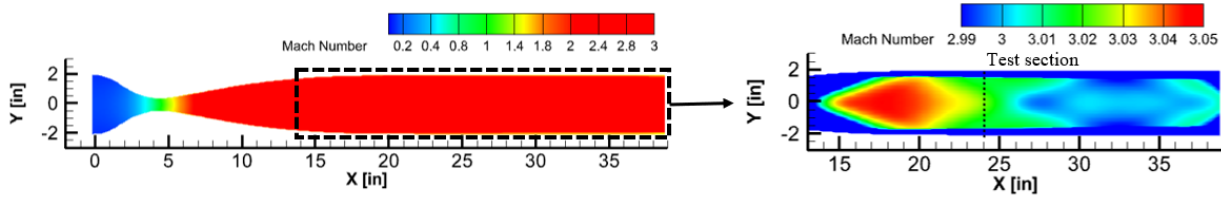


Figure 4.8 Contours of Mach number in Mach 3 nozzle through a) entire channel, b) test section ($p_0 = 100 \text{ psia}$).

System performance can be classified as adiabatic, but not entirely isentropic, as losses in total pressure are evident over the test section, causing higher numerical exit plane static pressures than predicted isentropically. This two-dimensional result validates the chosen nozzle designs by exhibiting minimal test section Mach number variation and promoting

Table 4.3 Numerical and Isentropic Test Section Parameters

	Mach 2 Nozzle		Mach 3 Nozzle	
	Isentropic expectation	Test section range	Isentropic expectation	Test section range
M_{TS}	2.072	1.987 - 2.034	3.123	2.984 - 3.043
$p_0[psia]$	45	45.1 - 45.8	100	100.4 - 103.3
$p_{TS}[psia]$	5.1408	7.256 - 7.937	2.266	2.810 - 2.889
$T_{TS}[K]$	161.4	164.4 - 168.6	101.7	105.8 - 108.0
$T_0[K]$	300	300.1 - 301.3	300	300 - 306.1
$\rho_{TS}[kg/m^3]$	0.7652	1.0603 - 1.1309	0.5353	0.6381 - 0.6426
$u_{TS}[m/s]$	527.7	516.6 - 522.7	631.3	622.5 - 626.1
$a_{TS}[m/s]$	254.7	256.9 - 260.3	202.2	205.6 - 208.2

flow uniformity by limiting the strength of shocks in this region. These results validate final nozzle contours and three-dimensional effects may be studied.

4.3.1 Three-Dimensional Computational Results

Three-dimensional computational validation has been performed and compared to the two-dimensional results to ensure design requirements have been met. Data pertaining to cross-sections along the test section length have been extracted so that 3-D corner effects on crossflow may be quantified. The extent of uniform core flow will be defined, as will the planar velocity distribution and its streamwise variation. These 3-D effects and corner vortex formation will be examined to ensure flow uniformity and angularity are maintained.

The distribution of Mach number and pressure over the nozzle and test section are obtained from the three-dimensional computational results, visualized in the contours shown in Fig. 4.10 - 4.15. These contours are taken along the centerline for the constant width (XZ plane) and expanding width (XY plane) for both Mach 2 and 3 nozzles along the streamwise direction to define the core flow uniformity and mean flow conditions.

The results are consistent with the two-dimensional results, with differences lying in an overall lower test section Mach number in the 3-D case, due to losses associated with three-dimensional corner effects. There is a gradual reduction in Mach number and associated increase in static pressure over the test section, as this flow as viscous effects lead to boundary

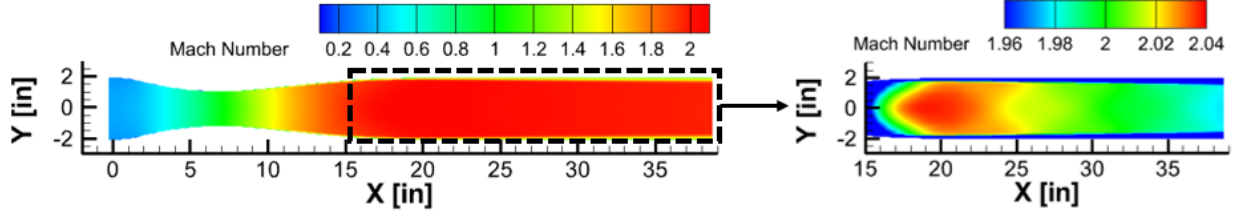


Figure 4.9 Contours of Mach number in Mach 2 nozzle along expanding width centerline plane through a) entire channel, b) test section ($p_0 = 45 \text{ psia}$).

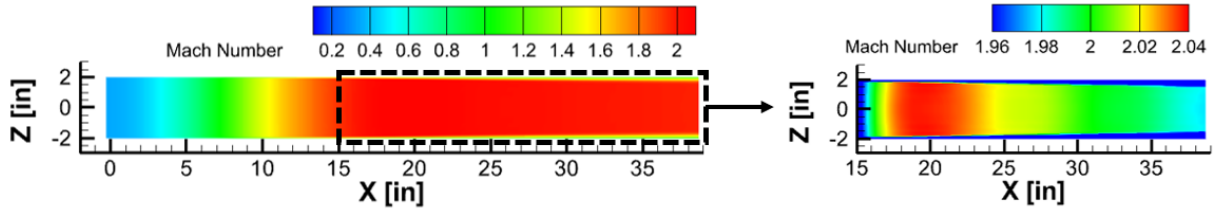


Figure 4.10 Contours of Mach number in Mach 2 nozzle along constant width centerline plane through a) entire channel, b) test section ($p_0 = 45 \text{ psia}$).

layer growth and frictional losses. The test section, which has a constant cross-sectional area, behaves like a classical Fanno flow in this capacity and minor losses are expected over this region. The constraint of parallel test section walls also induces some losses in the test section, as to satisfy a nominally isentropic flow, the flow will want to continue expanding after exiting the nozzle. Because it is forced to travel linearly through this region, there will be some weak oblique shocks that form in the test section as the flow is forced to continue linearly downstream. It is also evident that the Mach 3 nozzle displays a higher velocity and pressure gradient than the Mach 2 nozzle. Despite this, the gradient is not large in either instance, and it can be concluded that both nozzles satisfy the design requirement of establishing uniform flow through the test section, with losses that are minimal enough to establish a suitable test environment.

Centerline Mach variation is shown graphically in Fig 4.17. The flow is subsonic through the converging section, and accelerates smoothly to the sonic condition at the throat, at which the flow is choked and continues to smoothly accelerate through the diverging portion of the nozzle. Flow velocity reaches a maximum at the junction between the nozzle exit and

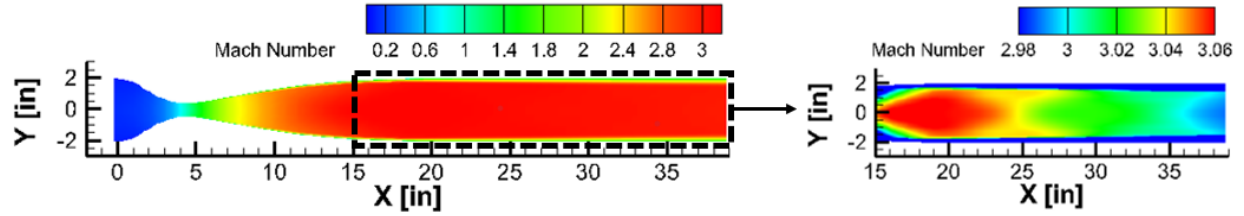


Figure 4.11 Contours of Mach number in Mach 3 nozzle along expanding width centerline plane through a) entire channel, b) test section ($p_0 = 100 \text{ psia}$).

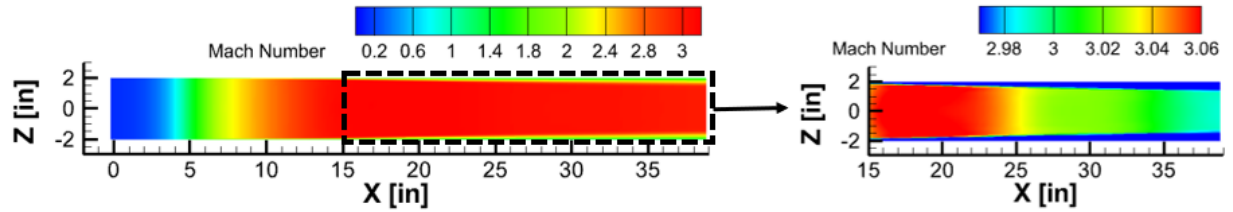


Figure 4.12 Contours of Mach number in Mach 3 nozzle along constant width centerline plane through a) entire channel, b) test section ($p_0 = 100 \text{ psia}$).

the test section, after which it decelerates slightly over the test section length as the channel area is held constant, as explained previously. The y-axis Mach range is reduced in Fig. 4.18 and 4.19 to show this trend.

Analysis of cross-sectional contours along the length of the nozzle and test section (XY plane) allow for the analysis of turbulent boundary layer development and determining the extent of the core flow reduction that occurs as a result of this phenomenon. It is essential to establish the boundary of the core flow so that the region of clean, uniform flow in which a model can be placed without being affected by turbulence can be determined. Boundary layer development and core flow variation are visualized through contours of Mach number at stations of interest in Fig. 4.20 - Fig. 4.21.

For both nozzles, the inlet Mach distribution shows a limited variation of entirely subsonic flow, as expected. The peak velocity occurs along the XZ centerline, with reduced velocity on the edges of the contoured surfaces. As there are no discontinuities in the flow, a smooth transition to sonic conditions can be ensured. As the flow is driven to the supersonic regime and the boundary layer develops through the diverging section of the nozzle, 3-D corner

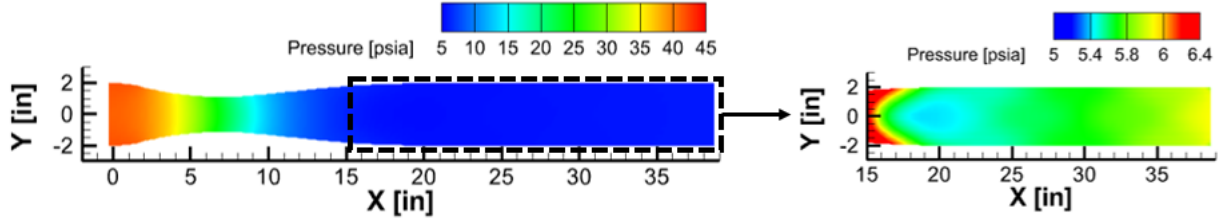


Figure 4.13 Contours of pressure in Mach 2 nozzle along expanding width centerline plane through a) entire channel, b) test section ($p_0 = 45 \text{ psia}$).

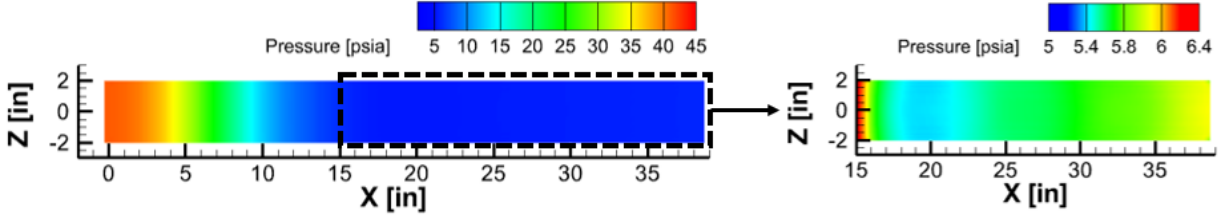


Figure 4.14 Contours of pressure in Mach 2 nozzle along constant width centerline plane through a) entire channel, b) test section ($p_0 = 45 \text{ psia}$).

effects begin to manifest, and can be seen in the nozzle exit cross section through the extent of the boundary layer at the nozzle exit plane. The boundary layer is found to be relatively thin in both instances, with the Mach 3 nozzle possessing a thicker boundary layer than Mach 2. Corner effects are manifested in a bowing inward of the flow, particularly in the sides bounded by the flat walls in the Z direction. The boundary layer development over the test section is evidenced in the cross-sectional contours at the test section exit plane. The extent of the boundary layer has visibly grown in this region relative to the nozzle exit plane. The corner effects have become more evident, particularly in the Mach 3 nozzle, with the high velocity region bowing inward along the XY and especially XZ centerlines, and extending closer to the walls near the corners. Again, however, the velocity variation is not significant and can be accounted for when positioning models in the test section to avoid interference of the boundary layer. It can be concluded that uniform test section flow conditions are established using both the Mach 2 and 3 nozzles generated.

As it is desired to produce a uniform flowfield with the velocity vectors directed along the X direction, crossflow was also analyzed by examining the magnitude of the velocity

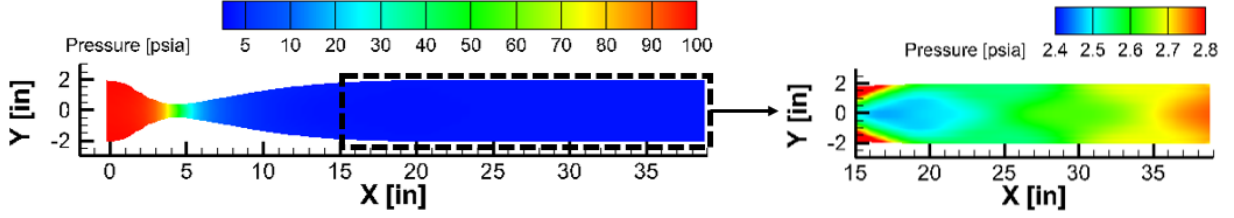


Figure 4.15 Contours of pressure in Mach 3 nozzle along expanding width centerline plane through a) entire channel, b) test section ($p_0 = 100 \text{ psia}$).

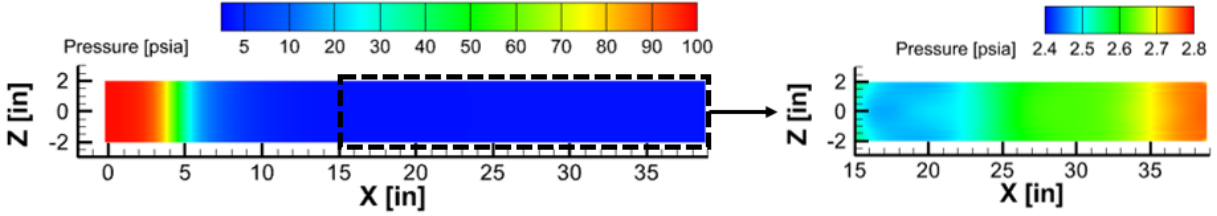


Figure 4.16 Contours of pressure in Mach 3 nozzle along constant width centerline plane through a) entire channel, b) test section ($p_0 = 100 \text{ psia}$).

component in the Z direction to ensure the streamwise velocity component is dominant along the length of the nozzle and test section. In the Mach 2 nozzle, the maximum magnitude of crossflow velocity is seen to be 0.0597 ft/s, as compared to the freestream velocity magnitude of 1716 ft/s. In the Mach 2 nozzle, the maximum magnitude of crossflow velocity is seen to be 0.0485 ft/s, as compared to the freestream velocity magnitude of 2054 ft/s. It can then be concluded that the crossflow effects are negligible as compared to the freestream values, resembling in-flight conditions.

To validate CFD simulations, numerical results were compared to expected values obtained with the isentropic equations. All values fell within an acceptable range for facility and instrumentation performance. The results of this comparison are tabulated below in Table 4.4.

4.4 Component Integration/Assembly

The full system overview is shown in Fig. 4.22. A round-to-rectangular transition piece will be mounted upstream of the nozzle to route the air from the circular stagnation chamber,

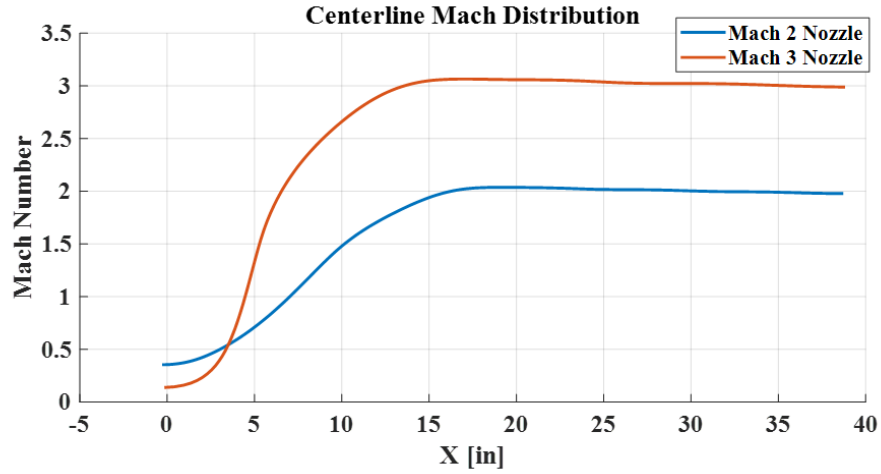


Figure 4.17 Centerline Mach distribution.

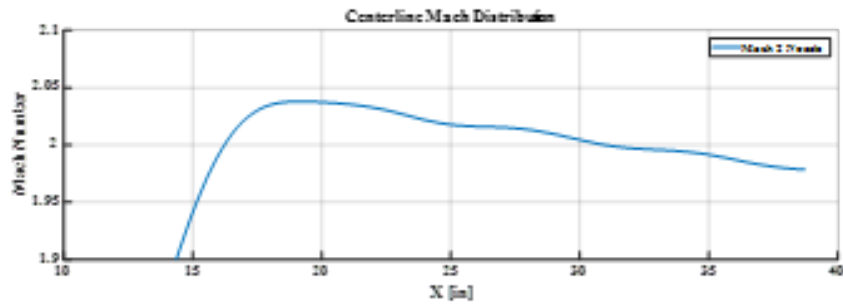


Figure 4.18 Centerline Mach 2 distribution.

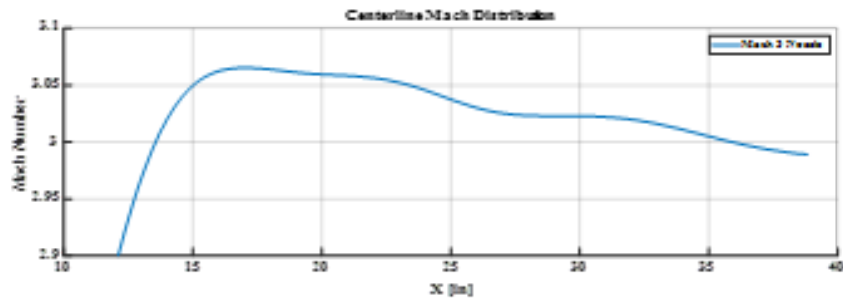


Figure 4.19 Centerline Mach 3 distribution.

within which mesh screens will be placed to minimize freestream turbulence. Downstream of the nozzle is the test section, which will have glass siding so that flow visualization may be performed. The diffuser section contains a second throat larger than the first to slow the flow before ejecting the air through a baffle exhaust system. Once this assembly is complete, experimental analysis of the flow properties will begin.

MACH 2

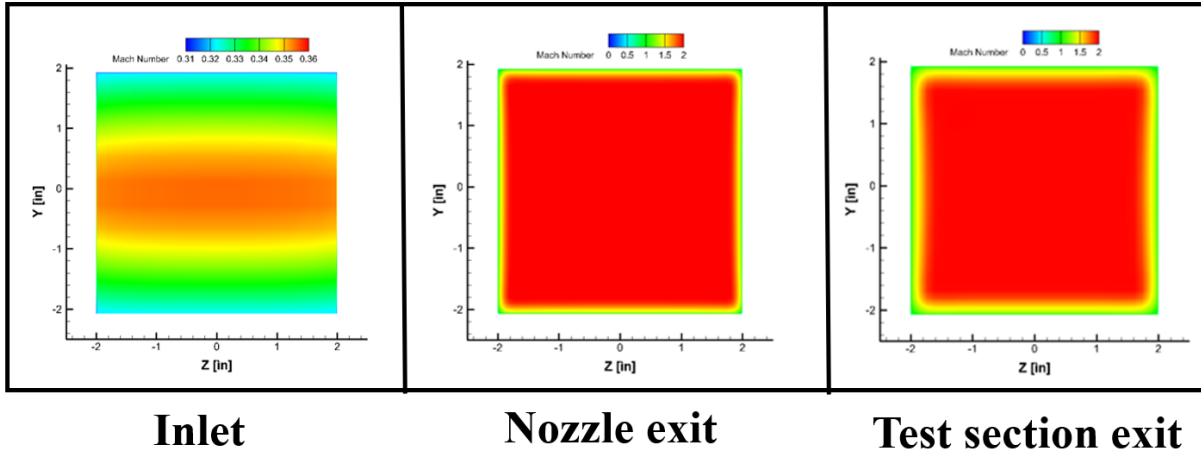


Figure 4.20 Contours of Mach number in Mach 2 nozzle along cross-sectional planes ($p_0 = 45 \text{ psia}$).

MACH 3

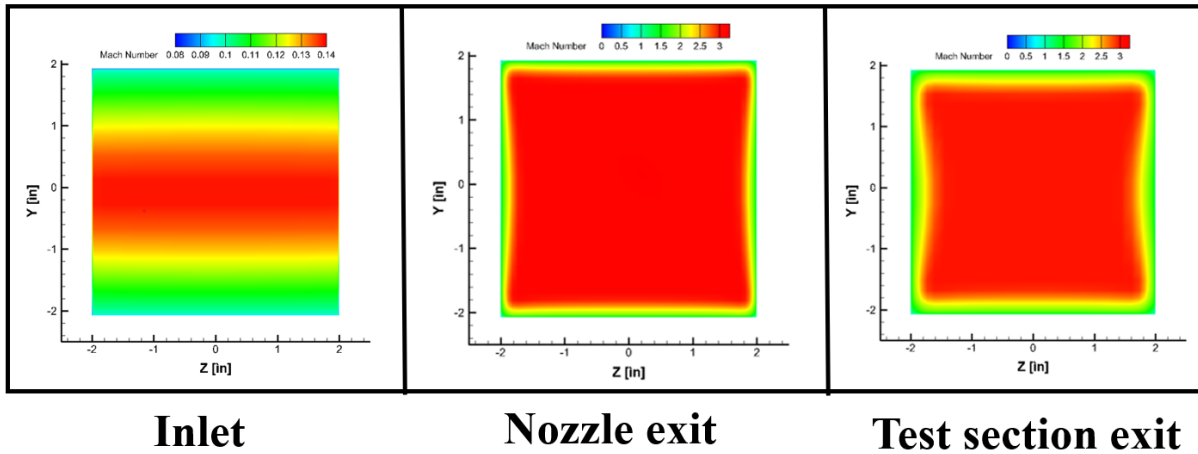


Figure 4.21 Contours of Mach number in Mach 3 nozzle along cross-sectional planes ($p_0 = 100 \text{ psia}$).

Table 4.4 Comparison of Numerical and Isentropic Exit Plane Conditions

	Mach 2 Nozzle		Mach 3 Nozzle	
Exit plane parameter	CFD	Isentropic expectation	CFD	Isentropic expectation
Velocity (M)	2.13-2.14	2.15	2.9-3.05	3.01
Absolute pressure	45325 Pa (6.57 psia)	34891 Pa (5.06 psia)	19325 Pa (2.8 psia)	21325 (3.1 psia)
Temperature	157 K (-177 °F)	156 K (-179 °F)	102 K (-276 °F)	106 K (-268 °F)

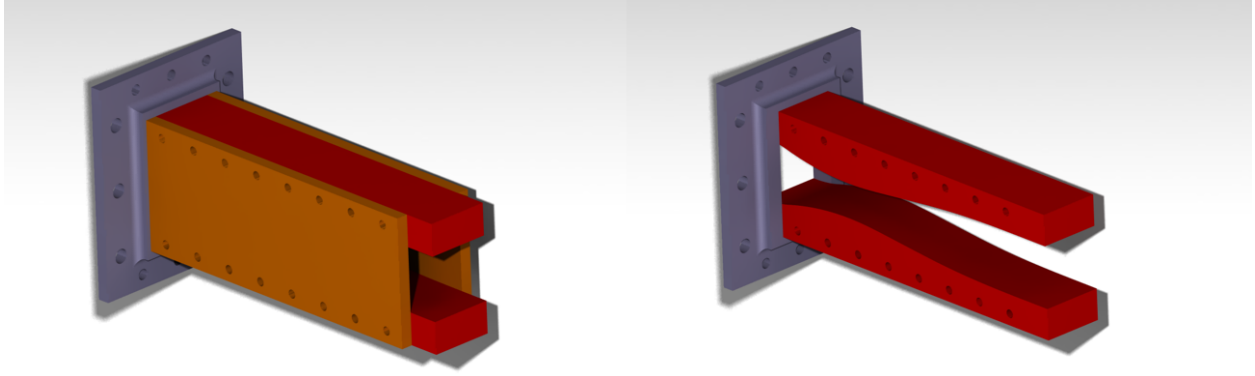


Figure 4.22 Nozzle solid model and assembly integration.

4.5 Nozzle Comparison

As compared to the currently possessed Mach 2.59 nozzle, the newly designed Mach 2 and 3 nozzles have shown considerable improvements in performance. The desired characteristics were to have cleaner flow in the test section, a larger test section, and reduce the adverse effects of the asymmetry. The contours of Mach number through the test section under the design condition for all nozzles, shown in Fig. 4.23 - 4.25, display the increase in flow uniformity, with less shock formation through this region and a much smoother and more limited variation in Mach number, quantified in Table 4.5.

The improvement in flow uniformity can also be seen by comparing the centerline Mach number over the nozzle length, shown in Fig. 4.26 - 4.28. The new nozzles have a much smoother expansion, while the old Mach 2.59 nozzle is characterized by discontinuities stemming from the shocks present in the nozzle.

The dimensions of the test section for the new nozzles $16in^2$ cross section, and 15 inches long, as compared to the current test section with a $2.2in^2$ cross section, and 3.5 inches in length. The new nozzles show a nearly 4 times more limited range in Mach number over a much longer test section, validating that the designs have been improved and a suitable test environment will be obtained in the new system.

Table 4.5 Comparison of Old and New Nozzles

	Mach 2.59	Mach 2	Mach 3
M_{TS}	2.45 - 2.67	1.97 - 2.03	2.99 - 3.05
Isentropic deviation	$\pm 5.4\%$	$\pm 1.5\%$	$\pm 1.6\%$
$p_{TS}[psia]$	5.0 - 8.4	5.7 - 5.9	2.6 - 2.8
$L_{TS}[in]$	3.5	15	15

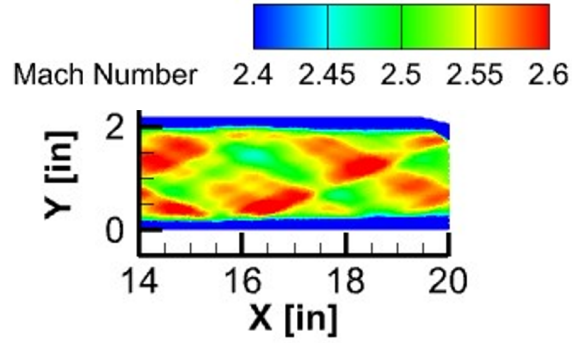


Figure 4.23 Mach 2.59 nozzle test section contours of Mach number.

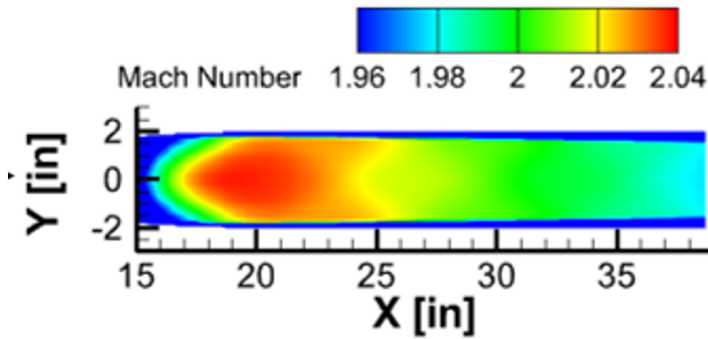


Figure 4.24 Mach 2 nozzle test section contours of Mach number.

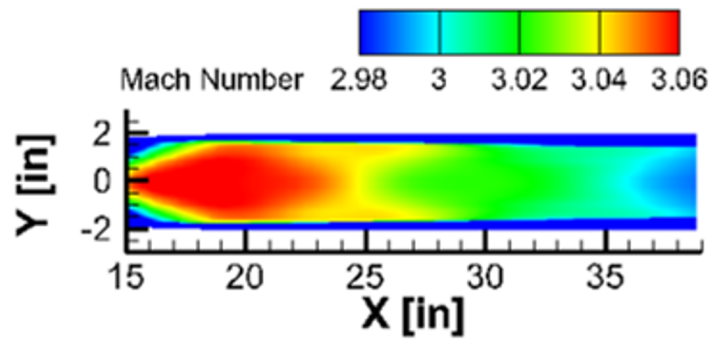


Figure 4.25 Mach 3 nozzle test section contours of Mach number.

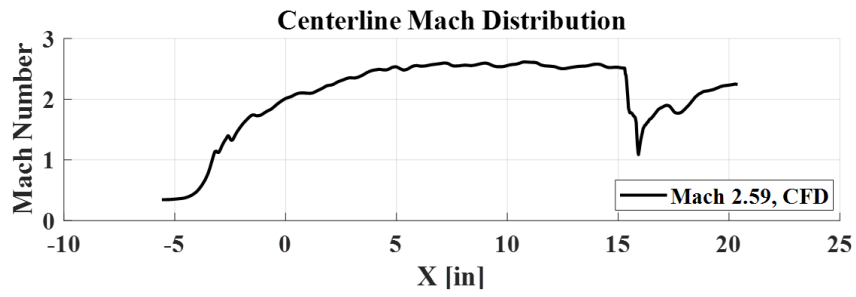


Figure 4.26 Centerline Mach number, Mach 2.59 nozzle.

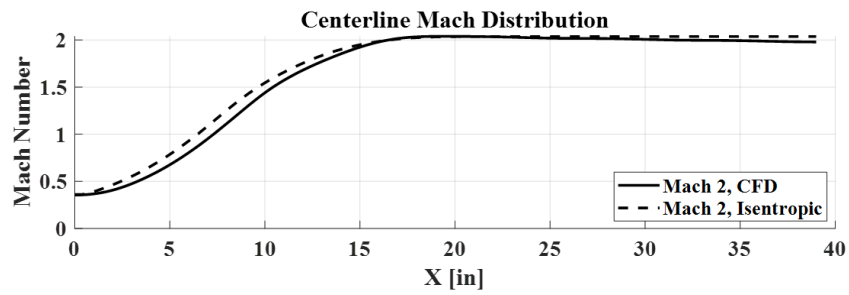


Figure 4.27 Centerline Mach number, Mach 2 nozzle.

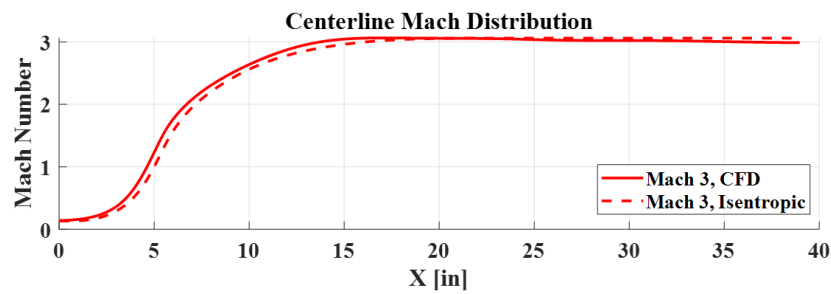


Figure 4.28 Centerline Mach number, Mach 3 nozzle.

5 Conclusions

This study has focused on the performance of supersonic nozzle flows, investigating the characteristics of these flows under both design and off-design conditions. Analytical and computational analysis, experimentation, and design of supersonic nozzles have been integrated to shed light on the complexities of these flows and the real consequences of viscous effects, shock interactions, and boundary layer development. This research has endeavored to decipher the challenges inherent in high-speed aerodynamics so that undesirable flow processes may be better controlled and the performance of vehicles operating within this regime may be improved.

5.1 Nozzle Overexpansion

The first portion of this study centered around the analysis of a Mach 2.59 planar nozzle operating in an overexpanded state. Current literature has illuminated the need for a higher level of understanding of overexpansion, as the instabilities and unsteadiness present in this viscous driven phenomenon lead to difficulties in predicting its defining characteristics, particularly the location and strength of the separation shock. Severe overexpansion has been seen to manifest in internal flow separation and the propagation of wave phenomena downstream of this separation. Numerical and experimental analysis of a nozzle operating at this state has allowed for the confirmation of these characteristics, and the associated complex turbulent structure has been visualized to highlight important patterns as the level of overexpansion is changed via changes to the NPR.

At low enough NPRs, the flow separates sharply from the internal nozzle surfaces. The back pressure is significantly higher than the exit pressure of the flow leaving the nozzle, and this pressure difference causes a region of entrainment that contaminates the internal flowfield. This separation is driven by viscous effects and is incited by a sharp separation shock forming off the nozzle wall, and thus this viscous overexpansion can be characterized by “shock-induced flow separation.” Incident separation shocks form on both nozzle walls and are connected near the nozzle centerline via a normal shock called the Mach stem. The Mach

stem was seen to be more pronounced at lower NPRs, with shorter angled incident shocks. The separation location was not constant, rather it oscillated along the streamwise direction. Immediately behind the Mach stem, a small region of subsonic flow is generated and then accelerated downstream. Behind the separation shock, the boundary layer separates from the nozzle wall, and a thin, highly turbulent free shear layer separates the subsonic recirculation region close to the wall and the core jet flow. A reflected shock extends from the triple point, which is in turn reflected from the free shear layer as an expansion wave, which is reflected as a shock, and so on, losing strength until it exits the nozzle.

The effects of the asymmetric nozzle configuration were evident in that the location of the incident separation shock was seen to occur further upstream on the flat surface than the contoured surface; the curvature of the nozzle promoted the delay of separation, and so it may be concluded that the separation was driven by the separation on the flat wall. Additionally, the recirculation regions have been shown to be highly asymmetric, with a large recirculation zone forming on the upper flat wall, and a much smaller separation zone on the lower contoured surface. It can be concluded that this is due to the earlier separation on the flat wall. This phenomenon seems to “push” the core flow downwards, which lies below the nozzle centerline throughout the nozzle and bends with the curvature of the lower wall.

Quantitative analysis of the pressure distribution within this nozzle has shown that the pressure distribution follows the isentropic expectation up until the point of separation, after which there is a sharp increase in pressure until the nozzle exit. The static pressure is seen to increase more drastically at lower NPRs, representing a stronger shock strength at more severe levels of overexpansion.

When comparing experimental to computational results, it is seen that modern standard two-equation turbulence models have yet to fully predict this phenomenon accurately and reliably. The strength of the separation shock was predicted with accuracy at high NPRs in the overexpanded regime using the k- ω SST turbulence model when compared to

experimental data, the separation shock strength and location of the separation were over-predicted, with numerical results showing the separation location to be further downstream than was actually seen.

5.2 Nozzle Design

In the next phase of the study of nozzle flows, Mach 2 and Mach 3 nozzles have been designed and analyzed numerically. A combination of methodologies have been utilized to generate optimal nozzle contours, including the MOC based Sivells' method for the diverging section, and the Hopkins-Hill formulation for the converging portion of the nozzle. CFD simulations using ANSYS Fluent validate the designs, showcasing the emergence of uniform flow fields within the nozzles. The success of the design strategy is evident in achieving desired flow characteristics. This precision in nozzle design ensured practical applicability of the nozzles for future use in a blowdown type supersonic wind tunnel.

Insights regarding three-dimensional effects on nozzle flows were made by analyzing the cross-sectional flowfields and boundary layer development through the nozzles and test section. The boundary layer growth through the test section has been shown to be more evident at higher Mach numbers, as are the 3-D corner effects. These effects are manifested in higher velocities near the corners of the nozzle and test section, with a slight bowing inward of the flow along the expanding-width and constant-width centerlines. These insights contribute to the refinement of design parameters, ensuring a more accurate representation of in-flight conditions.

The real-world implications of achieving successful supersonic flight underscore the practical relevance of the presented work. Nozzles are used in a wide array of flight systems, including jets, rockets, and wind tunnels. The demand for enhanced understanding and control of supersonic flows establishes the broader context within which this study holds relevance.

5.3 Recommendations

There is a great potential for this work to be continued; mechanisms driving nozzle flow characteristics can continue to be studied, and the newly designed nozzles will be integrated into a complete functional system.

Recommendations in regards to overexpansion include the continued use of different turbulence models in accurately predicting separation location. There are a variety of different two-equation models that may be compared to experimental data, and the proficiencies and shortcomings of each may be identified. A primary focus for continuing this work is to better characterize the overexpansion effects using time-resolved pressure measurements to better understand the underlying cause for unsteadiness in the separation location. The implementation of focusing schlieren is also recommended, so as to isolate a single cross-sectional plane along the streamwise direction of the nozzle. This will improve fidelity and eliminate any motion blur effects resulting from a classical Z-type schlieren setup.

The newly designed nozzles are intended for use in a new blowdown wind tunnel that is currently under construction. These nozzles should be constructed from aluminum, and be modular so that they may be switched out with ease to obtain a different Mach numbers in the test section. This unit process for nozzle design can be extended to any supersonic design Mach number, so the intent is that this process may be replicated and applied next to a Mach 4 nozzle to obtain even faster test conditions in the same facility. Future applications could also take form of a deeper exploration of three-dimensional effects and sensitivity analyses. These future directions aim to further refine our understanding of supersonic nozzle flows and bridge the gap between theoretical advancements and practical implementations.

Looking ahead, the focus remains on refining design parameters, unraveling three-dimensional intricacies, and translating findings into practical advancements. This research contributes to the ongoing narrative of high-speed aerodynamics, setting the stage for future innovations and facility development. The work presented here is not just a culmination of theoretical and computational efforts but a stepping stone towards advancing supersonic research.

6 REFERENCES

- [1] Schmucker, R. H., “Flow processes in overexpanded chemical rocket nozzles. Part 1: Flow separation,” Tech. rep., 1984.
- [2] Morrisette, E. L., and Goldberg, T. J., “Turbulent-flow separation criteria for overexpanded supersonic nozzles,” Tech. rep., 1978.
- [3] Lawrence, R. A., Symmetrical and unsymmetrical flow separation in supersonic nozzles, Southern Methodist University, 1967.
- [4] Hall, N., “Wind Tunnel Theory,” , May 2021.
URL <https://www.grc.nasa.gov/www/k-12/airplane/tunnoz.html>.
- [5] Anderson, J., EBOOK: Fundamentals of Aerodynamics (SI units), McGraw hill, 2011.
- [6] Smits, A. J., “Turbulent Boundary-Layer Structure in Supersonic Flow,” Philosophical Transactions: Physical Sciences and Engineering, Vol. 336, No. 1641, 1991, pp. 81–93.
URL <http://www.jstor.org/stable/53879>.
- [7] Bogdanoff, D., “Compressibility effects in turbulent shear layers,” AIAA journal, Vol. 21, No. 6, 1983, pp. 926–927.
- [8] Anderson, J. D., Modern compressible flow: with historical perspective, Vol. 12, McGraw-Hill New York, 1990.
- [9] Zebiri, B., Piquet, A., Hadjadj, A., and Verma, S., “Shock-induced flow separation in an overexpanded supersonic planar nozzle,” AIAA Journal, Vol. 58, No. 5, 2020, pp. 2122–2131.
- [10] Papamoschou, D., Zill, A., and Johnson, A., “Supersonic flow separation in planar nozzles,” Shock waves, Vol. 19, 2009, pp. 171–183.

- [11] Bourgoing, A., and Reijasse, P., “Experimental analysis of unsteady separated flows in a supersonic planar nozzle,” *Shock Waves*, Vol. 14, 2005, pp. 251–258. 68
- [12] Scheller, K., and Bierlein, J. A., “Some experiments on flow separation in rocket nozzles,” *Journal of the American Rocket Society*, Vol. 23, No. 1, 1953, pp. 28–32.
- [13] Hamed, A., and Vogiatzis, C., “Overexpanded two-dimensional convergent-divergent nozzle performance, effects of three-dimensional flow interactions,” *Journal of Propulsion and Power*, Vol. 14, No. 2, 1998, pp. 234–240.
- [14] Romine, G., “Nozzle flow separation,” *AIAA journal*, Vol. 36, No. 9, 1998, pp. 1618–1625.
- [15] Reshotko, E., and Tucker, M., “Effect of a discontinuity on turbulent boundary-layer-thickness parameters with application to shock-induced separation,” *Tech. rep.*, 1955.
- [16] Yaravintelimath, A., Raghunandan, B., and Morinigo, J. A., “Numerical prediction of nozzle flow separation: Issue of turbulence modeling,” *Aerospace Science and Technology*, Vol. 50, 2016, pp. 31–43.
- [17] Hunter, C. A., “Experimental investigation of separated nozzle flows,” *Journal of propulsion and power*, Vol. 20, No. 3, 2004, pp. 527–532.
- [18] Hamed, A., “High speed nozzles task,” *Tech. rep.*, 1995.
- [19] Geatz, A. M., “A Prediction Code for the Thrust Performance of Two-Dimensional, Non-Axisymmetric, Converging Diverging Nozzles,” 2005.
- [20] Deng, Y., “Design of a two-dimensional supersonic nozzle for use in wind tunnels,” *San Jose State University*, 2018.

- [21] Sivells, J. C., “A computer program for the aerodynamic design of axisymmetric and planar nozzles for supersonic and hypersonic wind tunnels,” US Air Force Arnold Engineering Development Center Rept. AEDC-TC-78-63, Arnold AFB, TN, 1978.
- [22] Settles, G. S., *Schlieren and shadowgraph techniques: visualizing phenomena in transparent media*, Springer Science Business Media, 2001. 69
- [23] Mazumdar, A., “Principles and techniques of schlieren imaging systems,” 2013.
- [24] Baird, S., Ephraim, A., and Singh, S., “Exploring the Influence of Off-Design Upstream Parameters on Supersonic Flow in de Laval Nozzles,” AIAA SCITECH 2024 Forum, 2024, p. 2343.
- [25] McCabe, A., “Design of a supersonic nozzle,” 1964.
- [26] Rao, G., and Beck, J., “Use of discontinuous exit flows to reduce rocket nozzle length,” 30th Joint propulsion conference and exhibit, 1994, p. 3264.
- [27] Plyashechnik, V., Byrkin, A., and Verkhovsky, V., “Gasdynamic design of shaped nozzles for supersonic wind tunnels, allowing for viscosity,” West-East High Speed Flow Field Conference, Moscow, Russia, Vol. 11, 2007, pp. 19–22.
- [28] Pope, A., and Goin, K. L., *High-speed Wind Tunnel Testing*, John Wiley Sons, Inc, 1965.
- [29] Korte, J., “Inviscid design of hypersonic wind tunnel nozzles for a real gas,” 38th Aerospace Sciences Meeting and Exhibit, 2000, p. 677.
- [30] Sivells, J. C., “Aerodynamic design of axisymmetric hypersonic wind-tunnel nozzles,” *Journal of Spacecraft and Rockets*, Vol. 7, No. 11, 1970, pp. 1292–1299.

[31] Hopkins, D., “Effect of small radius of curvature on transonic flow in axisymmetric nozzles.” AIAA Journal, Vol. 4, No. 8, 1966, pp. 1337–1343

PUBLICATIONS

- [1] **Baird, S.**, Ephraim, A., and Singh, S., “Characterization and Analysis of Supersonic Flow through de Laval Nozzles at Varied Upstream Design Conditions,” AIAA SciTech Forum 2024. <https://doi.org/10.2514/6.2024-2343>

- [2] Magnani, J., **Baird, S.**, et al., “Design and Flow Characterization of Noise Reduction System for a Supersonic Wind Tunnel,” AIAA SciTech Forum 2024. <https://doi.org/10.2514/6.2024-2839>

- [3] Mota, A., **Baird, S.**, et al., “Two and Three Dimensional Design and Characterization of Interchangeable Nozzles for a Supersonic Wind Tunnel Facility,” AIAA AVIATION Forum 2024. (not yet published).